MSc Thesis

Kinetics of the reductive dissolution of iron-containing by-products from drinking water treatment

Lourens van Langeveld

First supervisor: Thilo Behrends

Second supervisor: Mingkai Ma

Abstract

Phosphorus (P) losses from agriculture and industrial/urban waste to natural environments are ever-increasing, causing environmental damage and long-term P scarcity, which decrease biodiversity and food security respectively (Chen & Graedel, 2016, Cordell and White, 2013, Desmidt et al., 2015, Yuan et al., 2018). In natural systems, P mobility is largely governed by iron redox cycles (Li et al., 2012), hence, numerous iron products have been successfully applied to immobilise P in natural and engineered systems through sorption, and redox reactions (Bakker et al., 2015; Brennan et al., 2019; Cao et al., 2019; Cheng et al., 2015; Elliott et al., 2002; Koopmans et al., 2020; Li et al., 2012; Makris et al., 2005). Iron-containing by-products from drinking water treatment plants provide a low-cost, non-toxic, and bountiful source of such iron-oxides (Makris et al., 2005; Wang et al., 2013). Despite their proven efficacy, it remains largely unclear how heterogeneous mixtures of iron-oxides with varying properties behave throughout abiotic reductive dissolution processes. Obtaining a better understanding thereof is important, as the residency time in the target system is limiting to the reductive dissolution efficiency, and thus the P immobilisation efficacy, of the product.

This study set out to investigate the abiotic reductive dissolution capacity of 12 iron-containing by-products from drinking water treatment plants according to the methods from Postma (1993) and Larsen and Postma (2001) by applying a single kinetic model with a common set of parameters, k_{app} (initial reaction rate) and γ_{app} (iron-oxide assemblage reactivity), to the Fe(II) concentration evolution. Auxiliary analyses with XRD were used to determine the types of minerals present in each sample. Reductive dissolution kinetics could successfully be described by the rate law $J/m_0=k_{app}(m/m_0)^{\wedge}\gamma_{app}$, and significant differences could be observed between materials. The results indicate the iron-containing by-products to consist of one of three iron-oxide assemblages and were in order of most to least reactive: *Ca-dominated 2-line ferrihydrite > 2-line ferrihydrite > 6-line ferrihydrite and goethite*. The data suggests goethite exerts control over the terminal dissolution rate, whilst the initial dissolution rate is controlled by the least crystalline phase. Observed rate constants for 2-line Fh and 6-line Fh, transformed with the Arrhenius equation, were determined to be $k_{2\text{-}Fh} = 4.41 - 7.16 \cdot 10^{-4}$ s^{-1}, and $k_{6\text{-}Fh} = 4.56 - 7.44 \cdot 10^{-5}$ s^{-1}, similar to those determined by Larsen and Postma (2001). Despite our results only producing provisional trends, the knowledge that varying iron-containing by-products can be successfully described with a single kinetic model is valuable, and the potential for various applications is promising.

Table of Contents

1. Introduction

1.1 Phosphorus

Phosphorus (P) is an integral building block for life on earth and is becoming scarcer in both physical and economic terms, thus threatening global food security (Desmidt et al., 2015, Cordell and White, 2013). As opposed to the carbon (C), nitrogen (N), and oxygen (O) cycles, P cannot be cycled through the atmosphere since there exists no abundant gaseous form of it, which means in nature it is bound to becoming bioavailable through mineral weathering (Udert, 2018; Alewell et al., 2020). In other words, the global P cycle is relatively very slow, which means mined P from geological sources has to be used to artificially accelerate the natural weathering process. In absence, the inhibition of crop growth due to naturally low P availability would be limiting (Udert, 2018; Alewell et al., 2020). This, combined with the increasing use of non-renewable P and increasing scarcity of mineable P, is causing the global P distribution to further increase global P imbalances through soil and marine ecosystem losses (Bennett, 2001; Liu et al., 2018; Lun et al., 2018; Ngatia et al., 2019). In fact, of all extracted P, only an estimated 20% is consumed by humans, showing how severely inefficient our current systems are at not wasting this increasingly precious resource (Chen & Graedel, 2016). The accruement of P in aquatic environments as a result of P losses causes environmental damage and disruption through eutrophication (Alewell et al., 2020; Cordell and White, 2013). This has been established as a common issue across all marine environments (Carpenter et al., 1998). In the short-term, P run-off to bodies of water may cause the following cascade of events (1) toxic algae blooms, (2) anoxic events, (3) dead zones, and (4) a reduction in biodiversity, along with a decrease in water quality (Yuan et al., 2018; Ngatia and Taylor, 2018; Ngatia et al., 2019). Besides the environmental damage that P can cause, it is also causing significant geo-political instabilities, as newly found P deposits are often highly localised, causing other countries to have to import fertilizers whilst availability is low and prices are high (Alewell et al., 2020; Cordell and White, 2013)

It is, thus, in everyone's best interest to properly manage this resource in agriculture, industrial waste-streams, sewage, construction, and urban waste (Carpenter, 2008). The focus should not only be on the prevention of P eutrophication from these other waste-streams, but also on recovering and reusing the P within them (Chen and Graedel, 2016). Hence, in order to close the human P cycle, proper P management should extend beyond agriculture. By doing so through artificial immobilisation, recovery, and consequent reuse, a more sustainable P future can be assured. Increasingly popular materials for these purposes are iron-containing by-products from drinking water treatment processes. Over the last decades, they have gained traction as a desirable solution for mobile P binding in natural and engineered systems in an effort to mitigate eutrophication and stimulate P recovery and reuse.

1.2 Soil and sediment P

Although a significant portion of P is deposited in marine ecosystems, not all P is mobile, since a large portion is ab- and adsorbed to soil minerals, complexed with organic matter (OM), and present as soil-stable minerals (Alewell et al., 2020). This so-called *legacy P* can have significant long-term effects on the natural environment by water-induced soil erosion on longer time-scales (Alewell et al., 2020). Nevertheless, soils may have varying quantities of immobile and mobile P, which is dependent on affairs such as age, climate, and material (Wyant et al., 2013). For example, P retention as an immobile and thus lowly bioavailable fraction is most extreme in (1) old, eroded soils high in Fe-/Al-oxides and clays, where P sorption takes place, and (2) in carbonaceous alkaline soils where P forms soil-stable salts (Wyant et al., 2013). In principle, this means that depending on the location, fertilizers will also have varying ratios of their P contents leached, consumed, and immobilised (Wyant et al., 2013). The leached fraction may cause short-term issues such as eutrophication of marine ecosystems, whilst *legacy P* can have long-lasting effects by not being an abrupt but constant source of P for the hydrosphere

(Alewell et al., 2020; Bakker et al., 2015). This may prevent rehabilitation from eutrophicating conditions (Schindler et al., 2016). Nevertheless, it is thought that, as a result of the accruement of soil P from artificial fertilizers, the *legacy P* can cater as a potential resource for crop growth in the future. Interestingly, this indicates that although *legacy P* can have damaging long-term effects stemming from continued water-induced soil erosion, there is potential in using P activators which increase the bioavailability of this P (Alewell et al., 2020; Zhu et al., 2018). In lakes, the mobility of P can be similarly controlled by iron redox cycles. For example, in Lac Pavin, the tri-valent iron-oxides reduce to Fe(II) through OM assisted solubilisation in the anoxic layer of the lake (Busigny et al., 2016). At the redox boundary they again oxidize to Fe(III), which creates a concentrated layer of P-PO$_4$ rich iron-oxides. In addition, phosphates are mineralised with Fe(II), among others, as stable vivianite (Fe$^{2+}_3$(PO$_4$)$_2$·8H$_2$O) in the deeper sections of the lake. Thus, P is restricted to the anoxic parts as a result of iron redox cycling and can be immobilised by mineralisation under reducing conditions. Clearly, there are many external and internal factors governing P in soils and sediments, which calls for the need of proper P management strategies to prevent the loss of this resource through soil and mitigate the environmental effects it is already causing. Whether to control N or P (or both) in natural environments is an ongoing debate, but there is evidence that regulation of P in lakes can help reverse eutrophication (Conley et al., 2009; Schindler et al., 2016).

1.3 Fe-P interactions

Mobility of P in soils and sediments is governed by iron redox cycles, as P has a high affinity to adsorb to Fe(III)-(hydr)oxides, coprecipitate with Fe(III)-(hydr)oxides, or precipitate into Fe(II) phosphate minerals such as vivianite (Li et al., 2012). The reductive dissolution of Fe(III)-(hydr)oxides, where the materials solubilise and Fe(II) is released, is therefore often coupled with increased P mobilisation. Similarly, when vivianite is re-oxidized phosphate is released (Wilfert et al., 2015). However, this also means that under stable conditions, Fe(III)-(hydr)oxides can undergo reductive dissolution and consequently form various Fe-P precipitates that can remain stable and thus immobilise P on longer timescales. Likewise, Fe(III)-(hydr)oxides under aerobic conditions can adsorb and immobilize P for as long as they do not become reduced. This leads to the following events of Fe-P interactions (*Figure 1*):
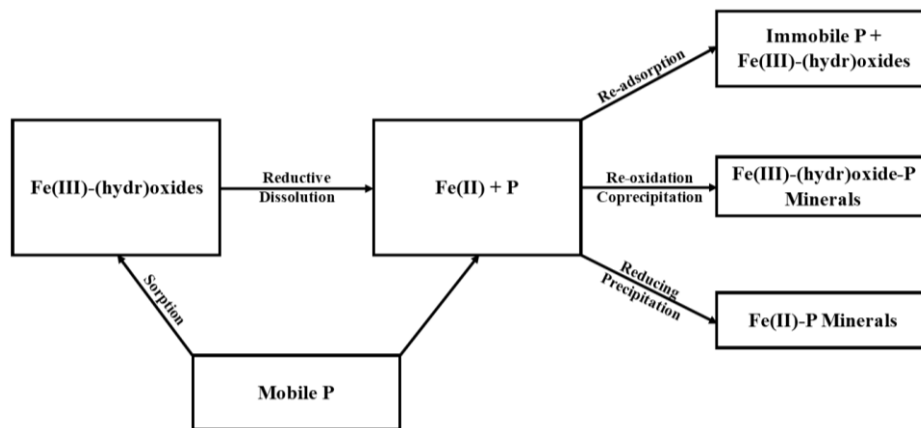
Figure 1: Reductive dissolution of Fe(III)-(hydr)oxides and possible pathways for P immobilisation.

1.4 Reductive dissolution capacity

Iron-oxides have been extensively studied for their role in P cycling and how they affect the nutrient's bioavailability due to the close coupling of iron redox cycling and phosphorus mobility (Hyacinthe and van Cappellen, 2004; Jan et al., 2015; Kraal et al., 2019; O'Connell et al., 2015; Slomp et al., 1996). The reductive dissolution that precedes mineralisation is a process that is controlled by three general

factors, namely iron-oxide reactivity, and reductant efficacy, which in turn is often catalysed by microbes (Postma, 1993). Since the reductive dissolution of Fe(III)-(hydr)oxides controls P mobility (among others), there is interest in understanding how capable the sediment and soil Fe(III) minerals are of dissolving. This iron-oxide reactivity is otherwise referred to as the reductive dissolution capacity. A number of studies, central to this paper, have demonstrated the ability to mathematically describe the reductive dissolution capacity of both monodisperse iron-oxide and polydisperse assemblages of iron-oxides from synthetic and natural sources by ascorbic acid (Postma, 1993; Larsen and Postma, 2001; Larsen et al., 2006), which can help elucidate the relative role of intrinsic iron-oxide properties in their own reduction processes. Consequently, this may provide new insights as to how fast Fe(II) for Fe-P mineral precipitation can become available, thus aiding in understanding the kinetics of the mechanism preceding P immobilisation. Very simply speaking, the faster the dissolution kinetics, the more Fe(II) available, the earlier Fe-P mineralisation can take place.

1.5 Iron-containing by-products from drinking water treatment

As has been established, one of the prerequisites for P immobilisation through Fe-P mineralisation in the environment is the initial reduction of Fe(III). In addition, P sorption to these materials can also add to the pool of immobile P. Therefore, iron products have long been an area of interest for the immobilisation and potential recovery of P (Ippolito, Barbarick, and Elliott, 2011; Wang et al., 2021). As a way to promote circular economies and use a low-cost material that is abundant, and non-toxic, iron-containing by-products from drinking water treatment plants may be used for the purpose of phosphorous removal from sediments, soils, and industrial systems (Makris et al., 2005; Wang et al., 2013). These products often consist of a variety of ferric iron hydroxides, oxides and oxyhydroxides (collectively referred to as iron-oxides) which can be present in several amorphous and crystalline phases (Wang et al., 2021).

Generally speaking, iron-containing by-products can consist of many different materials and is contingent on the source of the raw water, use of flocculants/treatment chemicals, and processing systems (Ippolito, Barbarick, and Elliott, 2011). The USEPA (2011) reported the types of processing systems chosen for the raw water treatment to be dependent on the water source and listed the following methods: pre-sedimentation, aggregation-sedimentation, precipitative softening, filtration, membrane-assisted desalination, ion-exchange, and adsorption through activated C (these are not mutually exclusive). They also indicate that, relatively, surface water tends to be higher in volatile/synthetic organic compounds, whilst groundwater contains more inorganics. Since surface water is high in organic matter (OM); aluminium, and iron-containing flocculants (such as iron-sulphates and iron-chlorides) are often used to remove these organic materials. Upon further oxidation of the surface water, the produced iron-containing by-products will therefore contain iron from exogeneous as well as endogenous sources, including a high OM content (Ippolito, Barbarick, and Elliott, 2011). Groundwater is often higher in iron concentrations (USEPA, 2011), which inadvertently means the iron-containing by-products are also richer in iron-oxides than those from surface water. Similar to groundwater is river bank filtrate, which essentially consists of surface water from which most inorganics, organics, and organisms are naturally filtered out prior to further treatment (de Vet et al., 2010). A more elaborate account of the water sources and production processes of the iron-containing by-products studied in this paper can be found in section *2.1 Studied iron-containing by-products*.

1.6 Applications of iron-containing by-products

Iron-containing by-products have been successfully used for P management in soils, marine sediments, lakes, and waste-water treatment processes. The following will provide a simplified account of some of the applications that have allowed for P immobilisation and recovery in natural and engineered environments.

In soils with low adsorptive ability, the aim can be to prevent P leaching from P-rich soils by artificially enhancing the P sorption capacity with iron-containing by-products (Koopmans et al., 2020). Koopmans et al. (2020) found they could be successfully applied to reduce orthophosphate solubility in a non-calcareous sandy soil. Similarly, in a batch-test comparison between aluminium, calcium, and iron-containing by-products, Elliott et al. (2002) found all could successfully immobilise P through sorption from triple-super-phosphate and biosolids-soil containing suspensions. Lastly, a soil-study by Brennan et al. (2019) indicated that not only did iron-containing by-products reduce the portion of water extractable P, they also did not add to the Mehlich-3 (weak acid extraction technique) extractable P. Thus, P leaching can be reduced by adding iron-containing by-products with the added value that they do not necessarily add to the pool of mobilizable P.

In sediments, the immobilisation of P with iron-containing by-products is somewhat different, the main objective is to reduce internal P loading (Bakker et al., 2015). This can be achieved through sorption, but also through P (co-)precipitation upon Fe(II) reoxidation or under continuous reducing conditions (Li et al., 2012). Wang et al. (2013) experimentally determined the quantity of water treatment by-products, containing iron and aluminium, necessary to immobilize phosphorous in lake sediments. In principle, adding iron to marine environments can be used as an efficient strategy to raise the supply of available iron, and thus increase the fraction of materials that control P mobility in these environments. By using these techniques, P cycling in lakes can be constrained, which allows for a faster recovery from eutrophicating conditions (Schindler et al., 2016).

Where in soils and sediments, the iron-containing by-product can be used directly, iron-oxides may be less favourable for P recovery from industrial P-rich waste-streams when used directly on oxidized effluent. This has to do with the difference in purpose: in soils and sediments this is immobilisation, whereas in waste-streams it should be recovery and reuse (Chen and Graedel, 2016). For example, when P from the waste-streams adsorb to the iron-containing by-products, they may have been immobilised to a specific phase in the effluent, but now the P has to be recovered from Fe-P complexes in order for it to be useful, which can prove challenging (Wilfert et al., 2015). Nevertheless, there are accounts of P recovery using various iron products. They have been successfully used in the removal of P from secondary wastewater effluent (Kang et al., 2008). A study by Wang et al. (2020) showed that the reduction of iron by bacteria plays a crucial role in phosphorus removal through vivianite production in sewage treatment plants. Similarly, Cao et al. (2019) reached high P recovery percentages in the form of vivianite from waste activated sludge fermentation. Lastly, research by Cheng et al. (2015) indicated ferrihydrite ($Fe^{3+}_{10}O_{14}(OH)_2$) reduction was of significant influence on the removal of P in anaerobically digested sludge, whereas hematite had no effect. These feats may also be achieved by reducing the iron-oxides in iron-containing by-products from drinking water treatment plants, which thus may provide a suitable source for reducible iron in these types of applications.

1.7 Research objective

Although the application of iron-oxides for the immobilisation of phosphorus in natural systems and the removal of phosphorus in engineered systems has been demonstrated to be successful, it is still largely unclear how heterogeneous mixtures of iron-oxides with varying properties behave. Their intrinsic reactivities may vary considerably due to the fact that the iron-oxides are produced from various raw waters and are often poorly defined and have low crystallinity. Specifically, the reductive dissolution kinetics as a result of these properties can differ significantly and, consequently, part of the iron-oxides might not be active if the time scale of reaction is shorter than the residence time in the intended application (such as the reactive part of a sediment or sewage treatment plant). As proposed by Wilfert et al., (2015) the lack of knowledge with regards to Fe/P chemistry in waste-water treatment is inhibiting the ability to use iron-rich materials as a strategy to recycle P.

The goal of this research was to determine the reductive dissolution rates of 12 iron-containing by-products from various drinking water treatment facilities, provided by AquaMinerals. Specifically, this study set out to determine whether the change and differences in rates as a result of mineral content and heterogeneity can be described using a single model with a common set of parameters of the form $J/m_0 = k_{app}(m/m_0)^{\gamma_{app}}$ (Postma, 1993; described in section *2.2 Kinetic model*). These may change as the samples can vary in composition and thus in individual properties. Therefore, sample characterisation through auxiliary analyses will be applied to explain the similarities and differences in reactivity of the samples in terms of initial/terminal dissolution rates and iron-oxide reactivities. This will principally be achieved by powder X-Ray Diffraction (XRD). Due to unforeseen circumstances, BET, EXAFS, and Raman data have not yet been collected. Nevertheless, X-Ray diffractograms will grant further insight into the mineral/chemical composition of the iron-oxides. This allows for the categorisation of iron-containing by-products in terms of reactivities. These parameters may eventually be used to infer which iron-containing by-product types are best applied in specific environments related to phosphorous binding in soils, aquatic sediments, and industrial waste streams, and pave the way for qualitative and quantitative indications of iron-containing by-product reactivity in these settings.

2. Background

2.1 Studied iron-containing by-products

The composition of iron-containing by-products that results from treating groundwater is strongly dependent on the properties of the infiltration area and the geology of the aquifer from which the water is extracted, as well as flocculants/treatment chemicals, and the processing systems applied (Ippolito, Barbarick, and Elliott, 2011). The following is an account of personal communication with Tonnie Hemme (Aquaminerals, 2021).

The groundwaters used to produce the samples that were studied in this paper are mostly anaerobic (*Table 1*) meaning many dissolved elements, such as Fe, Al, and Mn are present in a reduced form. One of the first cleaning steps is groundwater aeration, which causes dissolved species to oxidise and precipitate. This allows for sand/gravel filtration and subsequent sand/gravel washing, providing iron-containing by-products and filtrate. Depending on the groundwater chemistry, a drinking water production plant produces ranging quantities of these iron-containing by-products with varying compositions of oxidized inorganics and OM. Simply put, not one type of iron-containing by-product is similar to another when comparing individual locations.

In the case of riverbank water, the process is quite different, as is true for VITEW (*Table 1*). Here, the incoming water is semi-aerobic and is pre-filtered by a riverbank, hence the incoming raw water is called bank filtrate. Since this water is semi-aerobic, fewer reduced species will enter the treatment facility. Altogether, this means this type of raw water is expected to be low in suspended solids (de Vet et al., 2010). After initial filtration, the filtrate is aerated, and the oxidized solids are separated once more using sand/gravel filtration.

The surface water processed at PWNWPJ is a different story altogether (*Table 1*). Here, the incoming water is aerobic and usually contains high concentrations of organic matter (OM). Crude filtration steps are applied to remove larger debris, such as fish and refuse. In conjunction, pH adjustments are made to alkalize the water, aiding later flocculation processes (Pal, 2017). The OM content in the resulting suspension has poor settleability and thus needs to be aggregated through the addition of flocculants, which in this case are Fe(III) salts. The formed aggregates are isolated using lamellar separators, where the suspension cascades through inclined plates, leaving the solids to collect and slowly flow down into a receptacle at the bottom. This container can be emptied, providing iron-containing by-product that will mostly contain exogenous iron from the added flocculants together with OM.

Table 1: Overview of sample information and production characteristics

Initialism	Date	Company	Location	Source	Inlet water	By-product production	By-product separation
[-]	[dd/mm/yy]	[-]	[-]	[-]	[-]	[-]	[-]
BWVEG1	10/11/17	Brabant Water	Veghel	GW	AnA	Aeration	GF
BWVEG2	03/12/19	Brabant Water	Veghel	GW	AnA	Aeration	GF
EVBUHA	16/04/21	Evides	Burg-Haemstede	GW	AnA	Aeration	GF
EVHUI	21/04/21	Evides	Huijbergen	GW	AnA	Aeration	GF
PWNWPJ	29/11/19	Puur Water & Natuur	Andijk	SW	Aer	$Fe(II)SO_4$ $Fe(III)Cl_3$ as OM flocculants	LFS
VF14	?	Vitens	Leeuwarden (lab)	GW*	AnA	Aeration	GF
VF24	?	Vitens	Leeuwarden (lab)	GW*	AnA	Aeration	GF
VITBIL	23/04/21	Vitens	Bilthoven	GW	AnA	Aeration	GF
VITEEM	23/04/21	Vitens	Eemdijk	GW	AnA	Aeration	GF
VITEW	27/05/19	Vitens	Zwolle	BF	Semi-Aer.	Aeration	GF
VITVEE	13/04/21	Vitens	Veenendaal	GW	AnA	Aeration	GF
WMLB	20/04/21	Waterleiding Maatschappij Limburg	Bergen	GW	AnA	Aeration	GF

*GW – Groundwater, SW – Surface water, BF – Bank filtrate, AnA – Anaerobic, Aer – Aerobic, OM – Organic matter, GF – Gravel filtration, and LFS – Lamellar flow separation. *likely*

2.2 Kinetic model

In this paper, the methods used by Larsen and Postma (2001) and Postma (1993) will be closely followed, thus making this section a reiteration of the underpinning theories and mathematics from those papers, as together they form a very comprehensive document. These studies have successfully applied the following rate law (*Equation 1*) to explain the reductive dissolution behaviour of synthesized iron-oxides (ferrihydrite, lepidocrocite, and goethite), and oxidized marine and aquifer sediment containing a variety of particle sizes in the presence of an excess of L-ascorbic acid (henceforth referred to as LAH2) at a constant pH of 3. This paper will attempt to use their rate laws, and additional equations, to describe the reductive dissolution behaviour of iron-containing by-products stemming from the drinking water treatment processes previously described.

$$J = -\frac{dm}{dt} = km_0 F\left(\frac{m}{m_0}\right) S(C) \tag{1}$$

J is the dissolution rate in mol min^{-1}; *m* is the material mass in mol; *t* is the time in minutes; *k* is the first order rate constant of the initial material in min^{-1}; m_0 the material mass at *t* final in mol assuming Fe-OOH. This means that m/m_0 refers to the undissolved fraction of material, and thus does not have a unit. Therefore, the function $F(m/m_0)$ represents the iron-oxides that remain in suspension and describes the change in reactivity throughout the dissolution reaction. The function *S(C)*, on the other hand, represents

the concentration and type of reagent used to reduce the iron-oxides, in other words, the solution composition.

This means the rate law permits both functions to be studied individually. This can be achieved by keeping either one constant. In this paper, the solution composition *S(C)* is forcibly constant by adding LAH2 in excess, thus retaining roughly the same concentration throughout the dissolution experiments, with the important addition that the pH is kept constant at 3 as well. A verification of both can be found in section *3.2 Reactor design*. As a generic relationship, the function *F(m/m₀)* describes the reactivity of a monodisperse suspension of isometric particles, and may be expressed as *(m/m₀)ᵞ*, where γ = 2/3 given the change in reactivity over time in the strictest sense only captures the change in surface area and material mass (Larsen and Postma, 2001). However, it fully describes, beyond other effects, the decrease of interfacial area, particle dissolution, and a decrease in surface area. In most cases crystal suspensions will be polydisperse and not isometric, meaning the mathematically found γ value of 2/3 generally does not completely describe heterogeneous polydisperse dissolution reactions (Larsen and Postma, 2001). Nevertheless, *Equation 1* can be rearranged through the following steps to achieve equation (5).

$$k' = kS(C) \tag{2}$$

$$F\left(\frac{m}{m_0}\right) = \left(\frac{m}{m_0}\right)^{\gamma} \tag{3}$$

$$J = k'm_0 \left(\frac{m}{m_0}\right)^{\gamma} \tag{4}$$

$$\frac{J}{m_0} = k' \left(\frac{m}{m_0}\right)^{\gamma} \tag{5}$$

Then, it is assumed that the initial reactivity of a polydisperse suspension follows a gamma distribution function (*Equation 6*) containing parameters *a* and *v* (Boudreau and Ruddick, 1991).

$$g(\kappa, 0) = \frac{g_0 \kappa^{v-1} e^{-a\kappa}}{\Gamma(v)} \tag{6}$$

Boudreau and Ruddick (1991) have demonstrated that, in this case, the time evolution of *m/m₀* follows the relationship (*Equation 7*) for a reactive continuum of the decay of OM. This has successfully been applied by Postma (1993) and Larsen and Postma (2001) to instead describe a reactive continuum of iron-oxide dissolution.

$$\frac{m}{m_0} = \left(\frac{a}{a+t}\right)^{v} \tag{7}$$

Thus, in order to obtain the parameters *a* and *v*, merely the undissolved fraction of material *m/m₀*, and the time *t* are needed to perform data fitting, both of which are known from the reductive dissolution experiments. When considering the rate (*Equation 8*) belonging to *Equation 7* and the equation for the rate constant (*Equation 9*), substitutions can be made, simplifying to the rate law of *Equation 10*, which is very similar to *Equation 5*.

$$J = k_m m^{1+\frac{1}{v}} \tag{8}$$

$$k_m = \frac{v}{a m_0^{\frac{1}{v}}} \tag{9}$$

$$\frac{J}{m_0} = \frac{v}{a} \left(\frac{m}{m_0}\right)^{1+\frac{1}{v}} \tag{10}$$

The reactive continuum of iron-oxides can therefore be described through further substitution by the apparent rate constant (*Equation 11*) and the apparent materials reactivity/iron-oxide heterogeneity (*Equation 12*),

$$k_{app} = \frac{v}{a} \tag{11}$$

$$\gamma_{app} = 1 + \frac{1}{v} \tag{12}$$

which leads to the rate law

$$\frac{J}{m_0} = k_{app} \left(\frac{m}{m_0}\right)^{\gamma_{app}} \tag{13}$$

Importantly, the same form (*Equation 10*) of the rate law of *Equation 5* can describe the change in reaction rates using the progress of the reaction for both monodisperse, single-phase suspensions and polydisperse, multi-phase suspensions. The only difference is that in the latter case, the k_{app} (*Equation 11*) and γ_{app} (*Equation 12*) values have to be differently interpreted and reflect statistical parameters. This means that, when the obtained reductive dissolution data is fitted to *Equation 7* and values for parameters a and v are retrieved, they can be used to calculate k_{app} (*Equation 11*) and γ_{app} (*Equation 12*), thus providing the completed rate law *Equation 13*. These values allow us to interpret the reactivity of iron-oxides in natural samples. A higher rate constant (k_{app}) tends to imply the sample will have a high initial reaction rate, often controlled by the most reactive phase. In addition, for $\gamma_{app} \geq 1$, where the closer the value is to 1, the slower the reaction rate decreases throughout material dissolution, thus the more reactive the iron-oxides in the sample generally are and the more homogeneous the iron-oxide minerals tend to be. In principle, this means that because the rate laws can define all iron-containing by-product samples, and are normalised to the initial mass, the k_{app} and γ_{app} values can be directly compared. As a result, it is possible to categorise and even rank the samples in terms of initial reaction rate, terminal reaction rate and reactivity, among others.

2.2 L-ascorbic acid as a reductant

Besides the mathematics that explain the reductive dissolution kinetics, it is important to understand how the reductant LAH2 interacts with electron acceptors and how it can be used to track the reductive dissolution kinetics. The amount of iron-oxides that can be reduced by LAH2 within a set time-frame can be used as a proxy for bioavailable iron in sediments and soils, much like oxalate and dithionite extractions (Postma, 1993). Thus, in order to understand the reduction of iron-oxides in the iron-containing by-products, the reductive dissolution of Fe(III) can be forced using the same principle. LAH2 is an important human vitamin (vitamin C) and is often used in medicine for iron metabolism purposes, where it speeds up the reduction of Fe(III) and aids the Fenton reaction (Timoshnikov et al., 2020). The iron reduction process is coupled to a two-step LAH$^-$ oxidation reaction (*Figure 2*).
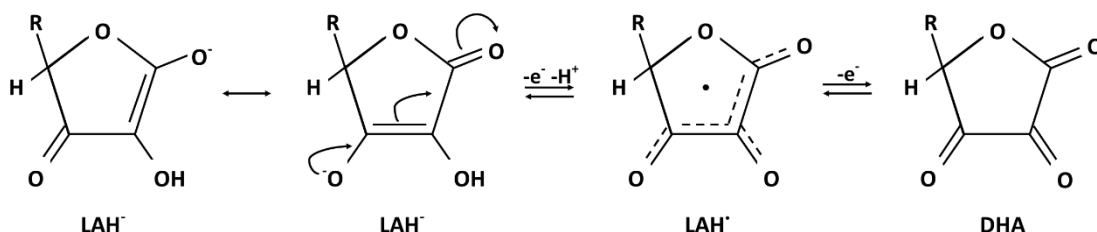

Figure 2: Two-step oxidation reaction mechanism of LAH$^-$, based on the reaction sequence from Linster and Van Schaftingen (2007).

First, the ascorbate anion that is formed when LAH2 is dissolved in water LAH$^-$ exchanges an electron with an electron acceptor, forming the ascorbyl radical LAH$^\cdot$. Radicals are energetically very unfavourable, and therefore also very reactive. In order to reach a more stable configuration, it will

donate another electron to an electron acceptor. Thus, it reaches the energetically favourable end product DHA, from which it could be subject to further degradation, although in pH ranges of 2-4 it is known to be stable for a few days (Shen et al., 2021). In the absence of oxygen, Fe(III) from the iron-oxides is used as an electron acceptor throughout this reaction. The generalized reaction for this process is given as *Equation 14* where the Fe(III) pool is represented by an iron-oxy-hydroxide (Fe-OOH).

$$2Fe(III)OOH + LAH2 \rightarrow 2Fe(II) + 4OH^- + DHA \qquad (14)$$

As the pH in the reactor is kept constant, any OH^- production from this reduction reaction will have to be met with equal H^+ addition. Therefore, *Equation 14* provides the basic stoichiometry of the overall reaction, which links the production of Fe(II) to the consumption of H^+. Given there may be other reactive and pH-changing species in the iron-containing by-products, the ratio between Fe(II) production and H^+ consumption can be used as an indicator for the occurrence of other H^+ consuming/producing reactions. The measured Fe(II) concentration evolution can thus be used to track the kinetics of the reductive dissolution of iron-containing by-products from drinking water treatment plants.

2.3 Relation between iron-oxide properties and intrinsic reactivity

As was introduced in the previous paragraph, the γ value is a collective descriptor of iron-oxide reactivity. However, there are many facets that dictate the reactivity of such materials in a controlled environment, the following list is probably far from exhaustive, but encapsulates some of the main aspects: composition, crystallinity, disaggregation, Fe(II) reactive site blockage, morphology, particle size distribution, reactive site density, and surface-mass ratio (Larsen and Postma, 2001; Li et al., 2012; Postma, 1993). In natural environments, this of course also includes variations in temperature, pH, and redox conditions. This section will briefly address a few of these controls on reactivity and how they relate to reaction kinetics.

Importantly, the material composition is of significant influence on many of the reactive controls. This is evidenced by the results from Larsen and Postma (2001) where the reactivity of iron-oxides based on initial reaction rates in decreasing order was determined to be *6-line Fh > 2-line Fh > lepidocrocite > goethite*, most of which are commonly found in iron-containing by-products from drinking-water treatment plants. In a review, Wang et al. (2021) reported that nano-crystalline hematite, goethite, and ferrihydrite can have high specific surface areas, where ferrihydrites tend to have the highest SSA, especially when not aged. A higher SSA implies more reactive surface would be available for reductive dissolution. In addition, Raiswell et al. (2010) found that as 2-line Fh ages, it aggregates increasingly, which significantly affects the dissolution kinetics by limiting the movement of the reductant into the intra-aggregate spaces, thus slowing down the reductive dissolution. This is also a factor of the particle size distribution and changing surface-mass ratios, where usually the smallest particles are dissolved first and the surface-mass ratio decreases, which also slows the reaction down over time (Larsen and Postma, 2001). A study by Erbs et al. (2008) found that the reductive dissolution rate of various sizes of 6-line Fh is proportional to the SSA, with the suggestion that observed differences in rate orders and pre-exponential factors (Arrhenius equation) were a product of the structure of water controlling the reductant diffusion rate to the reactive surface.

Not only do these intrinsic reactivities affect purely chemical processes, they also affect bacterial reduction processes. Bonneville et al. (2009) have determined a linear free energy relationship (LFER) between the solubility product of a variety of iron-oxides and initial reduction rates by *S. Putrefaciens*, where the lower the solubility product, the lower the initial reduction rate was. Hansel et al. (2004) showed that changes in surface reactivity of iron-oxides throughout microbial reduction regulates the reaction rates. Similarly, research by Roden (2003) indicated that the heterogeneity of the iron-oxide pool, which in this research is represented by the γ value, possibly controls initial bacterial reduction rates through changes in reactive site density.

Evidently, the intrinsic mineral properties control both chemical and biological iron reduction rates and are often interlinked. However, this paper only inquires upon the abiotic reduction of iron-oxides assemblages in iron-containing by-products, but results may be used to get an indication of the ease of dissolution by biological means as well.

3. Methods

3.1 Suspensions and solutions

Prior to obtaining iron-containing by-product for drying, the larger containers (i.e. buckets and bottles) were either agitated while closed by shaking or opened and stirred with a large steel spoon. In cases where the sample was liquid or only slightly viscous and at least not thick and clay-like, the containers were sampled using plastic pipettes. There where the samples were very viscous or clay-like, the containers were sampled using a large steel spoon. The aliquots were initially transferred to 50 mL conical PP centrifuge tubes (Greiner) to air-dry, but as the total evaporation of water would take days to weeks with this approach, a switch was made to air-drying in open-faced petri dishes, reducing the drying time to approximately two days. In events where even faster drying was desired, the petri dishes were transferred to an oven operated at 25°C with the fan at 70% capacity, which would usually result in a fully dried sample after one night. The low oven temperature was chosen as a means to prevent affecting the material. There is the possibility that some cross-contamination occurred during sample drying as the containers were usually open throughout the drying process. However, it is very unlikely that any minor dust transfer will have significantly affected the nature of the samples and thus the outcomes of the performed analyses. Dried samples shown in *Figure 3* are indicative of the variation of solids contents of all materials, but also differences between contents based on colour and drying pattern.
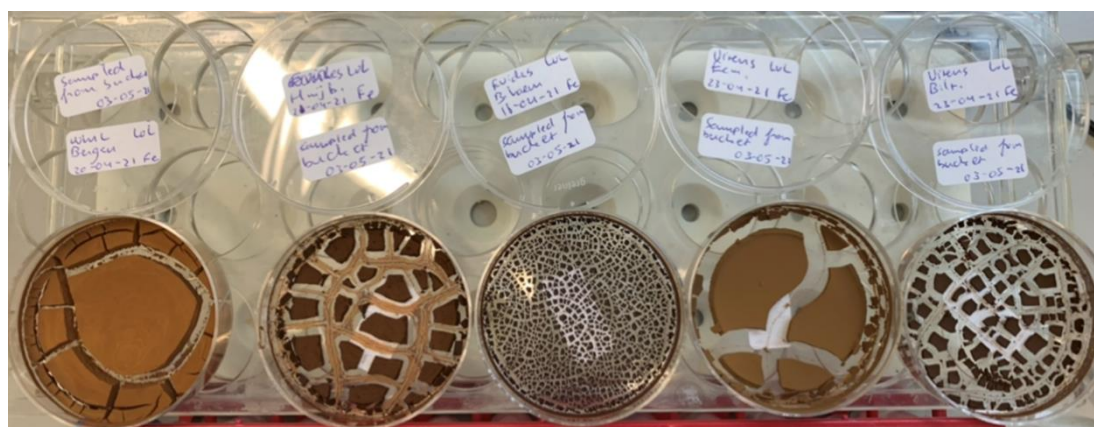

Figure 3: Dried samples of WMLB, EVHUI, EVBUHA, VITEEM, and VITBIL (left to right).

Dried materials were transferred to a mortar and pestle as a means to homogenize the samples, separate them from larger plant material, and reduce the particle size. Initially, this was achieved by grinding them along the walls of the mortar. However, we realised this may affect the crystal lattice, as the prolonged grinding may induce iron phase transformations. Therefore, all materials were resampled from their original containers, dried and then carefully crushed in the mortar and pestle. In some cases, this meant the particle size may have been larger, as some materials were more naturally fine-grained than others. We accepted the larger particle size of the initial materials in favour of minimizing the possibility of changes to the iron-oxide mineralogy.

In preparation for a reactor experiment, 0.0133 grams of sample was transferred to a 15 mL conical PP centrifuge tubes (Greiner), after which it was suspended in 1 mL of ultra-pure water. This would hydrate the material to ensure all of the material was available for reaction and hydration was not a completely uncontrolled limiting factor (Erbs et al., 2008). In cases where the grain size was relatively large, the sample would be crushed in suspension using a pipette tip to bring the grain size down.

Initially, the LAH2 solutions were prepared by weighing 0.2642 g of the salt directly into the Teflon reactor, and then weighing an additional 150 g of ultra-pure water to obtain 150 mL of 10 mM LAH2 solution. However, this was a rather time-consuming method of preparing a batch reactor run.

Therefore, in later stages, 15 mL conical PP centrifuge tubes (Greiner) were prepared with approximately 0.2642 g of LAH2. When needed, the content of one vial was rinsed out into the Teflon reactor using approximately 150 g of ultra-pure water. This would roughly yield 150 mL of 10 mM LAH2 solution. Since LAH2 is supposed to be in excess with respect to iron-oxides, it was not necessary to be very precise with the concentration, as long as it approximated 10 mM.

Since LAH2 readily reacts with oxygen, and thus degrades, it is important to have a system that is consistently near-anoxic or has a sufficiently high enough LAH2 concentration where the influence of oxygen becomes negligible (Oey et al., 2006). Thus, our reactor was constantly purged using N_2 gas to minimize this oxidation in the long term. Besides the presence of oxygen, the operating temperature is also an important factor. Oey et al. (2006) showed that LAH2 degradation occurs mostly as the result of dissolved oxygen (*Equation 15*), and once all oxygen is consumed the anaerobic degradation that continues takes place at a much slower rate.

$$LAH2 + \frac{1}{2}O_2 \rightarrow DHA + H_2O \tag{15}$$

Closest in relation to this study is their assessment of LAH2 stability at a concentration of 750 μg/L and an initial O_2 concentration of 8.1 mg/L, which approximates the O_2 saturation in pure water at STP conditions. Their assessment was made at a temperature of 100°C. The data suggests that after 35 minutes, approximately 18% of the LAH2 had degraded. However, the reactor in this study is operated at 60°C and contains approximately 1760 μg/L LAH2 but is operated for approximately five or more hours. Although it is not clear from the study by Oey et al. (2006) whether the LAH2 degradation is concentration dependent, the lower temperatures and higher LAH2 concentrations may make the initial effects of dissolved oxygen in our reactor negligible. Especially considering the prolonged anoxic environment from continuous N_2 gas purging, meaning only anaerobic LAH2 degradation will be available, besides the degradation caused by the iron-oxides. Therefore, it can be assumed that the concentration of LAH2 will remain in excess relative to the concentration of reducible iron throughout the reactor experiments.

The ferrozine reagent (R1) was prepared by dissolving 0.493 g of the monosodium salt hydrate of ferrozine in 100 mL ultra-pure water to obtain a solution of 10 mM. Then, 0.771 g of ammonium acetate ($C_2H_7NO_2$) was added to reach a solution concentration of 100 mM ammonium acetate. This recipe can be scaled depending on how much reagent is needed.

In order to obtain a 5 M ammonia buffer solution (R3) using ammonium acetate, 77.08 g of this salt was dissolved in 200 mL of ultra-pure water. The pH was adjusted to 9.5 using an ammonium hydroxide ($NH_3 \cdot H_2O$) solution. This recipe can also be scaled.

To make an Fe(II) calibration series, an Fe(II) stock solution (R4) was first prepared by dissolving 0.3921 g of ammonium-Fe(II)-sulphate-hydrate (($NH_4)_2Fe(SO_4)_2 \cdot 6H_2O$) in 100 mL of 0.1 M HCl to obtain a concentration of 10 mM Fe(II). Then, ten standards from 0 μM to 50 μM in steps of 5 μM were prepared, and the ferrozine method (as described in the next paragraph) was followed. This produced the calibration series in *Appendix A*.

The following section describes how to perform the ferrozine method, possible pitfalls, and overall chemistry as per Stookey (1970). In the experiments in this paper the monosodium salt hydrate of 3-(2-pyridyl)-5,6-bis(4-phenylsulfonic acid)-1,2,4-triazine, otherwise known as ferrozine, was used for the colourimetric determination of free Fe(II) ions in solution (*Figure 4*). This organic reagent complexes with divalent iron to form a stable magenta complex between pH 4-9, of which the absorbance can be measured at λ = 562 nm (*Figure 3*).
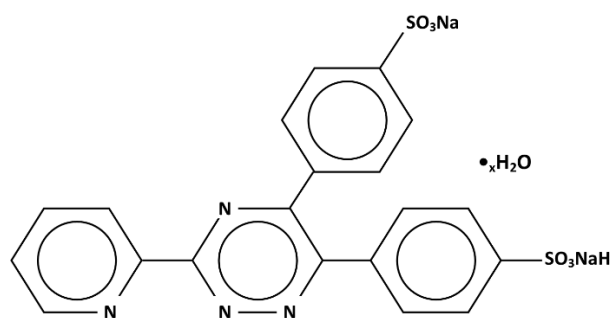
Figure 4: Organic structure of the monosodium hydrate salt of ferrozine, the structure is based on Stookey (1970).

Besides Fe(II), it is known to complex with other divalent and non-divalent species as well as colloidal particles and other solids. Therefore, it is important to use a very fine filtration method to remove most solids and reduce interference. However, dissolved species other than Fe(II) may always cause interference in the measurements, which may need to be considered for data analysis. As was shown by Stookey (1970), species such as Co(II), Cu(I), and CN$^-$ can cause significant deviation from true Fe(II) concentrations, but this appears to require concentrations of these species to be equal to, or higher than, the concentration of Fe(II) in solution. Given the source of the iron-containing by-product samples studied in this paper, it is highly unlikely that there were any non-iron species in solution at significantly interfering concentrations (USEPA, 2011). Furthermore, the pH of 3 and anoxic conditions at which the reactor was operated do not promote a significant presence of Fe(III). In conclusion, measured absorbances can be assumed to belong solely to the presence of Fe(II).

Prior to experiments, the spectrophotometer was turned on for at least half an hour to pre-heat the light source. Meanwhile, a series of semi-cuvettes was prepared with ultra-pure water for dilution of the reactor solution samples (usually 10X dilution for the first 30 minutes of sampling and 20X dilution for the remainder of the reactor run). When the spectrophotometer was ready for use, a separate semi-cuvette containing over 1.5 mL of ultra-pure water was inserted and the instrument was blanked. When measuring a sample, the appropriate volume of filtered reactor solution was added to the ultra-pure water in the prepared semi-cuvette to reach a total volume of 1.3 mL. Then, 200 μL of ferrozine solution (R1), and 400 μL of buffer solution (R3) were added in succession. The semi-cuvette was closed with a lid and the contents were homogenized, after which the absorbance was immediately measured. An example of a measurement series, together with the calculations, can be found in *Appendix B*.

3.2 Reactor design

A double-walled glass sleeve, connected to a Haake DC10 immersion circulator and K20 refrigerated water bath thermostat, containing a Teflon beaker insert was used as the batch reactor vessel. Initially, the reactor was operated at 25°C, but after a few test-runs it became clear the reaction may take days or even weeks to reach completion. Henceforth, the reactor would be operated at 60°C, allowing for the bulk of the reaction to reach completion within approximately 5 hours. The Teflon beaker was fitted with a 0.1 M HCl Metrohm 809 Titrando and 800 Dosino pH-stat combination supplied with a Metrohm Profitrode (6.0255 110) electrode to keep the pH constant at 3. In addition, a nitrogen duct was fitted to the reactor to promote an anoxic environment at all times. Although the reactor was not air-tight, the reaction was not expected to be significantly oxygen sensitive, especially not at the pH at which the reactor was operated. Each experiment was conducted using 150 mL of 10 mM LAH2 to which various iron-containing by-product suspensions were added, granting iron-oxide concentrations of <1mM. The vessel contents were constantly mixed with a Teflon stirring bar and a Hanna HI 190M stirring plate. Stirring rates were non-specific, as it was not always practically possible to use the same speeds across batch experiments. Instead, an appropriate stirring rate was chosen that was high enough to homogenize the reactor contents, whilst not risking the stirring bar straying from its trajectory and hitting the pH-electrode. A picture and diagram of the reactor can be found in *Figure 5*. Reactant concentrations and

experimental set-up used in this study were largely based on the parameters and auxiliary content from Postma (1993).
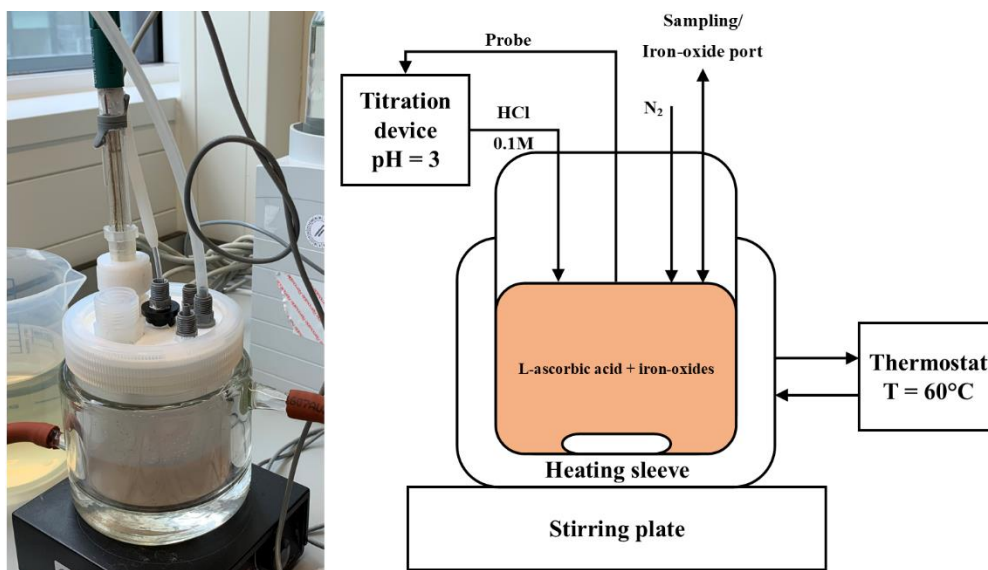

Figure 5: A picture of the reactor with complementary diagram including all facets of the reactor.

However, it is important to note that the reducible iron content of the materials was variable. This means that, although the same mass of different samples was used in the batch experiments, the results had to be normalized to individual reducible iron content m_0 to allow for comparison. The initial objective was to achieve this through HCl digestion experiments. Despite this experiment producing unusable results, it was possible to instead use the iron concentration measured at the final time-point of a reactor experiment. This still provided a value for reaction progress and should not affect the trajectory of the Fe(II) evolution over time. Given LAH2 was present in excess, more than 20x the stoichiometric equivalent of iron-oxide (see *Equation 14*) continually saturating the solid-liquid interface, it is unlikely for the varying total reducible iron content to have caused significant changes in the reaction rate. This was verified by performing a simple litmus test; adding extra LAH2 after completion of one of the batch experiments had not increased the Fe(II) concentration, whilst adding fresh iron-containing by-product immediately caused the Fe(II) concentration to rise. This implied the reaction rate was not LAH2 limited, nor had the considerably high temperatures in the reaction vessel caused significant LAH2 degradation. Instead, the reductive dissolution kinetics were only expected to change as a result of matters such as reactive surface, material composition, and maturity. Therefore, although the reducible iron content of each material varies, it was still possible to produce results that could be compared under the same conditions by calculating the Fe(II)/Fe(fin) fraction, which is the reduced iron concentration normalized by the concentration measured at the final experiment time-point.

3.3 Reactor operation

Prior to a batch test, the Teflon reactor and stirring bar were cleaned with ultra-pure water and 70% ethanol, and dried using paper towel (or acetone when available). The reactor and stirring bar would be inspected for any leftover iron-oxides from previous runs to ensure no exogeneous material could interfere with the measurements of the impending reactor run. The stirring bar was added, and a vial containing 0.2642 g of LAH2 was rinsed out into the reactor using an ultra-pure water wash bottle, resulting in approximately 150 mL of 10 mM LAH2 solution. A lid containing plastic tubing that would sit below the solution level for nitrogen diffusion was screwed onto the reactor, and the assemblage was transferred into the heating sleeve. Afterwards, the thermostat was turned on to circulate water at 60°C and preheat the reactor, a nitrogen duct was fitted to the reactor lid allowing for nitrogen flow through the solution, and the stirring plate was turned on to homogenize the solution. The reactor was purged with nitrogen and heated to 60°C for at least an hour prior to injecting the iron-containing by-product suspension. This would ensure a fully anoxic and consistently heated solution. Meanwhile, the pH-probe was recalibrated using two solutions of pH 3.998 and pH 7.018 at a temperature between 20-21°C, and the titration device and software were prepared. Afterwards, the pre-hydrated iron-containing by-product (0.0133 g in 1 mL of ultra-pure water) was transferred into a pipette tip, measuring both the weight of the sample tube before and after the fact (this data was used to determine the fraction of iron-containing by-product left in the sample tube). When the reactor solution was fully heated and nitrogen-purged, the probe was inserted into the reactor and the pH was adjusted to 3.000 using 0.1M HCl in the titration device. Due to the first deprotonation of LAH2 to LAH$^-$, the reactor solution would start at a pH of approximately 3.15. The second titration sequence was started, and the iron-containing by-product suspension was injected into the reactor. A first sample was always taken after the first minute, after which samples were taken whenever considered fitting, with the requirement that the density of measurements is highest in the first hour of the reactor operation as this is where the initial reactivity can be tracked. A Pasteur pipette was used to sample approximately 1.5-3 mL of suspension from the reactor and then immediately transferred to a syringe where the plunger had been removed and an MDI Nylon-66 0.20 μm disc-filter had been fitted to the spout. The plunger was placed back in and the first mL of solution was expelled into a waste vat, after which the remaining filtrate was dispensed into a small (1.5-2 mL) centrifuge tube. Using a pipette, 250 μL of filtrate was transferred into another small centrifuge tube containing 25 μL of 6M HCl solution. The filtration would stop the reaction by removing particulate iron-oxides and the concentrated HCl would prevent the filtrate from oxidizing, which would otherwise have led to Fe(II) to Fe(III) transformation. The resulting samples were analysed using the Ferrozine method (Stookey, 1970).

3.4 Data fitting procedure

Data fitting was performed by closely following the non-linear least squares (nls) method explained by Kemmer and Keller (2010) to *Equation 7* using real-time Fe(II) evolution data. In Excel, the differences between the real-time data and fitted data at the measuring time-points was squared, the sum of which provided the SSR. The Excel Solver function was then instructed to freely vary the parameters *a* and *v*, which changed the resulting values for the fitting function *Equation 7*, provided the condition that the SSR → 0.000001. The solver function was repeatedly applied until the SSR remained constant. The found parameters, *a* and *v*, were then be used to calculate k_{app} (*Equation 11*) and γ_{app} (*Equation 12*), which provided the completed rate law (*Equation 13*). A sensitivity analysis of the kinetic model can be found in *Appendix C*.

3.5 Thermogravimetric Analysis

Thermogravimetric Analysis (TGA) is a destructive method where a sample is heated, and weight changes are recorded as a function of temperature increase. This can provide information on adsorbed/structural water, dehydroxylation processes/polymorphic phase transitions, and melting transitions. In this study, samples of between 0.5 and 3 grams were heated at a rate of 1°C per completed step in weight change from 0-1000°C in a LECO TGA-701.

3.6 Decalcification and TOC

Total Organic Carbon (TOC) measurements provide information of the percentage of organic carbon relative to the total weight of a sample. Measurements were done using an Isotope Ratio Mass Spectrometer (IRMS) together with Gas Chromatography Combustion (GC-C), which burns the OM in a sample, providing a signal that can be compared to an internal standard. The iron-containing by-product samples had earlier been determined to contain carbonates, which had to be removed prior to TOC analysis, as otherwise the signals of OM and Inorganic Carbon (IC) would compound, and essentially provide a Total Carbon (TC) measurement. Hence, decalcification steps were taken, ensuring only OM carbon and other non-dissolvables remained. An empty 15 mL conical PP centrifuge tube (Greiner) was weighed, after which approximately 0.3 g of dried iron-containing by-product sample was measured, and the tube was reweighed. Then, the dried iron-containing by-product was suspended in 7.5 mL of 1 M HCl and subsequently centrifuged at a speed of 2100 RPM for 10 minutes, after which the supernatant was discarded. This process was repeated twice, after which the sample would be resuspended in 7.5 mL of 1 M HCl and placed on a shaker table at 110 RPM for 3 hours. Again, the sample was centrifuged at 2100 RPM for 10 minutes, and the supernatant was discarded. The sample was then resuspended in 7.5 mL of 1 M HCl and placed back on the shaking table at 110 RPM for 4 days. Afterwards, the supernatant was decanted, and the sample was washed using the same technique as applied with 7.5 mL of 1 M HCl, but instead using 10 mL of ultra-pure water and repeating the process four times. The sample tubes and respective caps were transferred to a 60°C oven for at least 4 days to dry. Upon completion, the centrifuge tubes were removed from the oven and the caps were immediately screwed on. The weight of the centrifuge tubes was recorded, providing the weight-loss from dissolvables. In a number of cases, it turned out this technique did not only dissolve carbonates, it also dissolved almost all of the iron-oxides. This led to most centrifuge tubes only having a fleck of OM residue left, which was by far not enough to measure TOC. Perhaps these methods of OM determination and decalcification are not suitable for iron-containing by-product, as its contents are simply too sensitive. A different approach may have to be applied in which TIC is measured, after which TOC is measured, both with untreated samples. This should provide the fraction of carbonates in a sample, as well as the total C in a sample. Substituted, the results should approximate the total organic carbon.

3.7 XRD and micronisation

Powder X-Ray Diffraction is a technique that allows for the qualitative interpretation of distinct diffraction patterns that belong to specific minerals. Peaks obtained with this method can be compared with a database (in this study, the PDF-4 reference) containing characteristic arrangements, where filtering can be achieved more easily if the general chemical composition of the measured material is known. If done properly, the bulk contents of the sample in question can be ascertained. In addition, when the grainsize is small enough (i.e. crystallite size), the particle size can be calculated from the diffraction data and even the crystallinity can be determined.

The main instrument used was a Bruker-AXS D8 Advance, fitted with a LYNXEYE XE-T detector and a Cu K-α cathode operating at $\lambda = 1.54060$ Å. Measurements were performed in steps of $0.020465°2\theta$ at 0.85 seconds per step over a range of $3-70°2\theta$. The sample was measured with a variable slit set at 20 mm and a 2.5° soler slit, whilst the powder mount rotated at 15 rpm. Software used to control the instrument and interpret the data was Diffrac.eva. All samples were measured using a side-loaded random powder mount. This assured random crystal orientation, whilst promoting close material packing and few empty gaps, increasing the data output quality.

Dried and pre-crushed iron-containing by-product samples were ground to crystallite size (<10 µm) using the micronisation XRD-Mill McCrone. Isopropyl alcohol was used to keep the sample cooled and reduce dust formation during the milling process. Temperature reduction during mechanical milling is important to retain the crystal lattice, as is keeping the energy input from the milling process low enough. Even though a study on the effect of milling of blue-dust, which contains mostly hematite, determined a phase change to wüstite (FeO) to take 50 hours (Sakthivel et al., 2014), we wanted to make absolutely sure that our materials remained minimally affected. Unfortunately, to our knowledge research concerning the effects of micronisation on the crystallinity and phases of iron-oxides is very scarce. Chong et al. (2021) used the same mill type for the purpose of iron-oxide micronisation and found when comparing sieved and milled iron-oxides using SEM, there were few differences, with the exception of the milled products expressing some localised rough-spots. To verify the mineralogy would remain unaffected by the micronisation process, a comparison test was performed between a mortar and pestle crushed material, and a micronized material, both from sample EVBUHA (*Figure 6*).
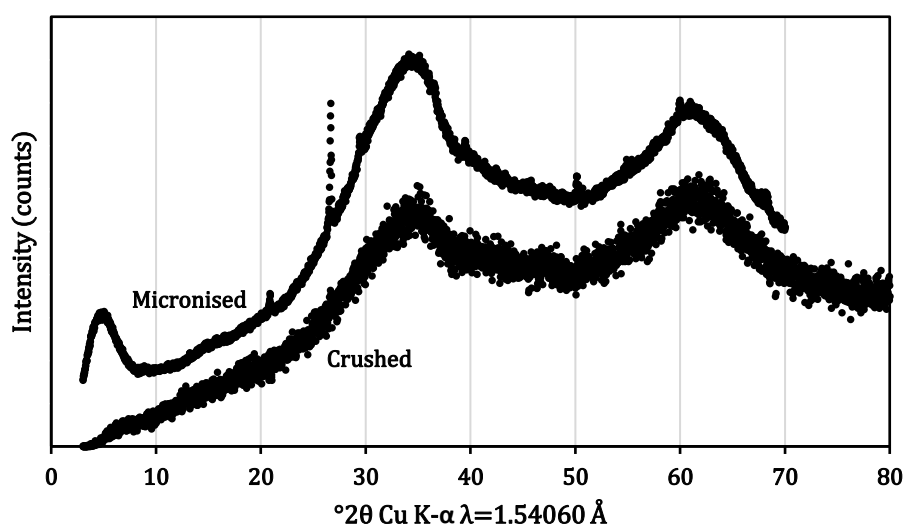

Figure 6: Comparison between X-Ray diffractograms of crushed, and micronised iron-containing by-product from EVBUHA. No artificial intensity offset has been implemented; these represent raw intensity data.

The data in *Figure 6* indicates both diffractograms contain general 2-line Fh structures (Drits et al., 1993), where the micronised material produced a higher overall intensity. However, the crushed

material does not show other material peaks, nor does it produce the characteristic Fe diffraction band below 10°2θ. The micronised material on the other hand shows this band, and also has indications of characteristic peaks for calcite and quartz. Calcium-carbonate phases preceding calcite, such as amorphous calcium carbonate and vaterite, are unlikely to have been present prior to micronisation, as these are highly unstable in natural environments and transition rapidly into the more stable calcite (Nehrke et al., 2006). Similarly, quartz is unlikely to have materialised and thus crystallised from other phases as a result of micronisation. Therefore, the data suggests that the micronisation process has not affected the iron-containing by-products, but instead has made their contents better visible by increasing their diffraction capacity. This can be explained by the original material being rather coarse in comparison to the micronized material, thus the micronized material would provide a more tightly packed sample providing more dense and levelled volume to measure, which is a requirement for the sample to be representative (Mos et al., 2018). In fact, we can conclude that in order to be able to analyse all iron-containing by-products more accurately with Cu cathode XRD, the micronisation process is invaluable in visualising data that may otherwise be poorly visible.
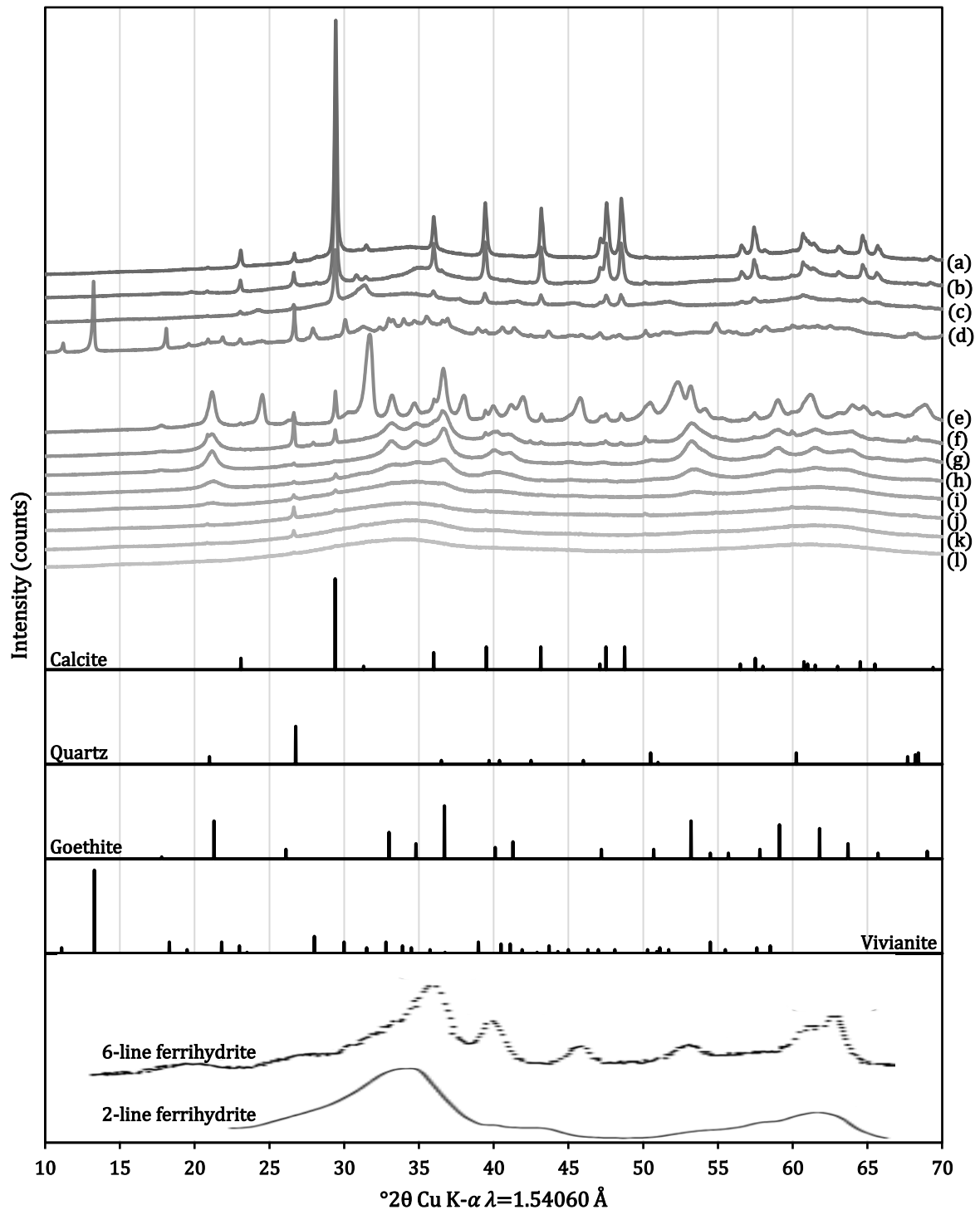
4. Results

4.1 XRD

Figure 7: Stacked (y-offset trivial) X-Ray Diffractograms of samples BWVEG1 **(a)**, WMLB **(b)**, BWVEG2 **(c)**, VITVEE **(d)**, PWNWPJ **(e)**, VF24 **(f)**, VF14 **(g)**, EVHUI **(h)**, VITEW **(i)**, EVBUHA **(j)**, VITBIL **(k)**, and VITEEM **(l)**. Below the experimental data are approximated characteristic peak positions and approximate relative peak heights (within respective diffractogram) of main determinable components based on the PDF-4 reference. Experimentally determined diffractograms for 6-line Fh and 2-line Fh were adopted from Drits et al. (1993) and are exaggerated relative to the other diffractograms.

The data from the X-Ray diffractograms indicate that, although most iron-containing by-products originated from the oxidation of anaerobic groundwater, there can be significant differences in composition between samples (*Figure 7*).

Table 2: Mineral contents of all iron-containing by-products determined from the X-Ray diffractograms in *Figure 7*.

Mineral Formula	Quartz SiO_2	Calcite $CaCO_3$	2-line Fh $Fe^{3+}_{10}O_{14}(OH)_2$	6-line Fh $Fe^{3+}_{10}O_{14}(OH)_2$	Goethite $Fe^{3+}OOH$	Vivianite $Fe^{2+}_3(PO_4)_2 \cdot 8H_2O$	Baricite $(Mg,Fe^{2+})_3(PO_4)_2 \cdot 8H_2O$	Siderite $Fe^{2+}CO_3$	Oligonite $Fe^{2+}(Mn,Zn)(CO_3)_2$
BWVEG1 (a)		X	X						
WMLB (b)		X	X						
BWVEG2 (c)		X	X						
VITVEE (d)	X		X			X	X	X	
PWNWPJ (e)				X	X			X	X
VF24 (f)	X			X	X				
VF14 (g)				X	X				
EVHUI (h)				X	X				
VITEW (i)			X						
EVBUHA (j)			X						
VITBIL (k)			X						
VITEEM (l)			X						

Calcite and quartz were observed in all samples, but a few samples had exceptionally intense peaks for either mineral. These samples are the only ones indicated as containing calcite or quartz in this table.

The X-Ray diffractograms indicate the samples principally consisted of either 2-line Fh and calcite, 6-line Fh and goethite, or only 2-line Fh, and can thus be categorised accordingly (*Table 2*). This means most iron-containing by-products were dominated by Fe(III) minerals. Individual 6-line Fh has not been determined to be present in any of the samples and was always paired with goethite. 2-line Fh and goethite have not been found together in any of the X-Ray diffractograms, whereas diffractograms dominated by calcite appear to only contain 2-line Fh as the other prevalent material. In case of samples BWVEG1, WMLB, and BWVEG2, the diffractograms were dominated by the presence of calcite. The only true outliers are sample VITVEE where the data indicates the presence of vivianite, baricite, and siderite, and sample PWNWPJ where there are indications of siderite and oligonite, all of which happen to be reduced iron minerals. Peaks from goethite sometimes caused difficulties in ascertaining whether the other mineral in the sample was indeed 6-line Fh. However, its characteristic peak at 1.98Å does not interfere with any goethite peaks, meaning the presence of 6-line Fh could be determined more confidently. Nevertheless, it is important to keep in mind that Mos et al. (2018) have shown that the use of a Cu cathode, instead of a potentially more suitable Co cathode, can muddy the data resolution through an increased background caused by X-Ray fluorescence.

4.2 TGA

Rather than plotting the weight-loss curves as a function of temperature (TGA), the first derivative of this data was plotted providing the change in weight-loss per unit of time (dW/dt) as a function of temperature (T in °C), also called a Differential ThermoGravimetric (DTG) curve (*Figure 8*).
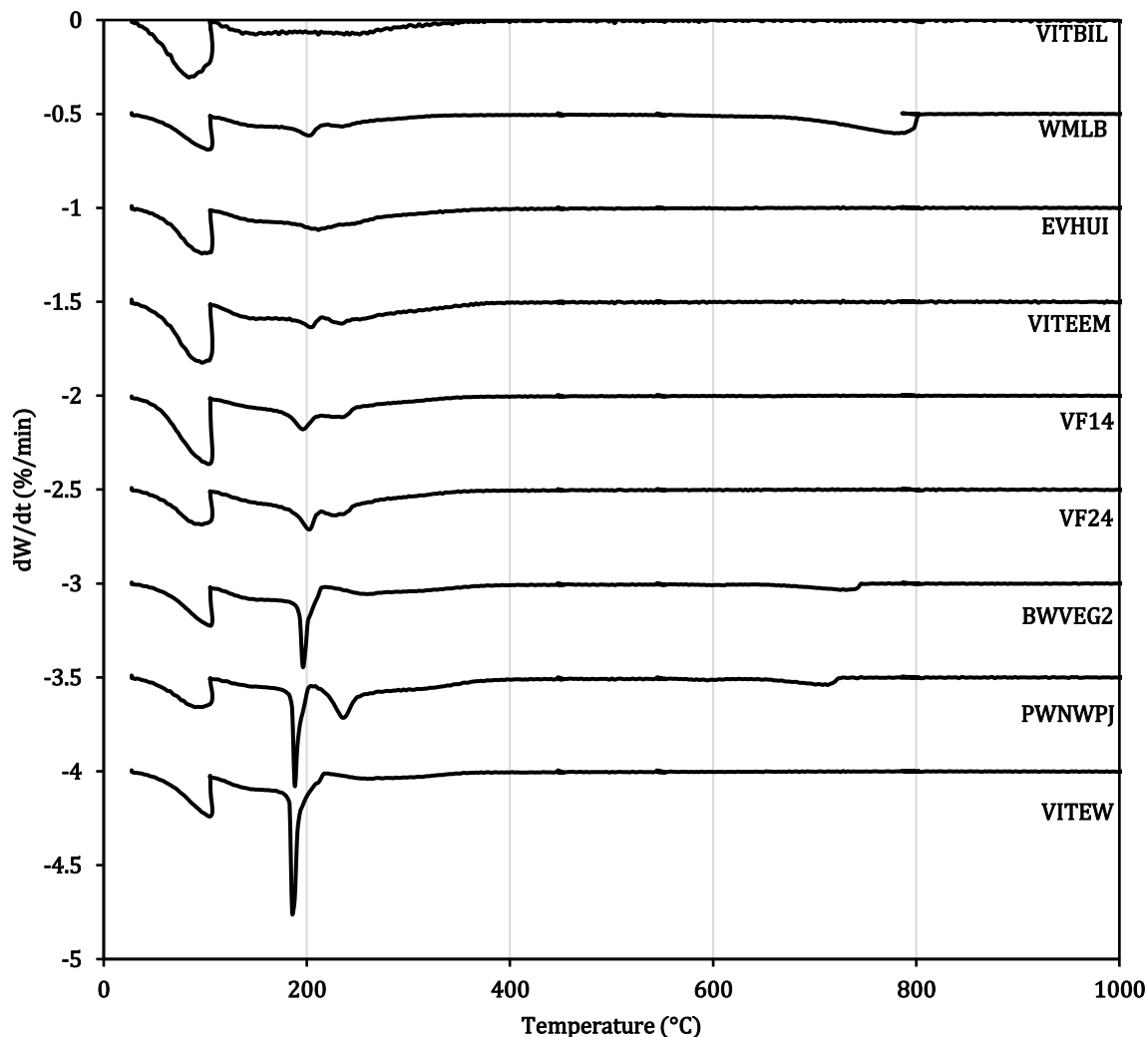

Figure 8: Differential Thermogravimetric data for VITBIL (k), WMLB (b), EVHUI (h), VITEEM (l), VF14 (g), VF24 (f), BWVEG2 (c), PWNWPJ (e), and VITEW (i). Data y-offsets result from $dW/dt - 0.5 \cdot n$, where $n =$ *alphanumeric equivalent*. Structural and adsorbed water loss is usually recorded below 200°C, dehydration and dehydroxylation between 200-400°C, and carbonate phase transformation above 600°C.

TGA data informs the samples have very similar graphs, typically consisting of two broad peaks between approximately 27-105°C and 105-400°C. The second broad peak may contain one or two additional sharper peaks, the first of which was found with its peak position between 185-205°C, and the second was found between 230-250°C. In some cases, a broad peak was observed above 600°C. Generally, structural, and adsorbed water loss is recorded below 200°C, dehydration and dehydroxylation between 200-400°C, and carbonate phase transformation above 600°C (King et al., 2015). However, these are only estimations, and there may be variations in these ranges. The data then suggests the peak between 27-105°C was produced by adsorbed water loss. The following broad peak with optional sharper peaks is a typical indication of structural water loss/dehydroxylation reactions. Remaining peaks after 600°C are typical for carbonate phase transitions, where structural carbon dioxide is removed from the material. Interpretations of these peaks will be discussed later on.

4.3 Kinetic experiments

4.3.1 Testing phase

Initial tests were conducted using two different reactor concentrations of iron-containing by-product from WMLB. Both batch experiments contained approximately 150 mL of 10 mM LAH2 solution and individual material concentrations of 0.11 mM and 2 mM. Here, it was assumed that all added material was present in the form of Fe-OOH, thus the Fe(II) concentration was normalized to the total material concentrations in the reactor. This approach was chosen because the data indicated neither experiment had reached (near-)completion, which was determined by the lack of asymptotic behaviour of the recorded data.
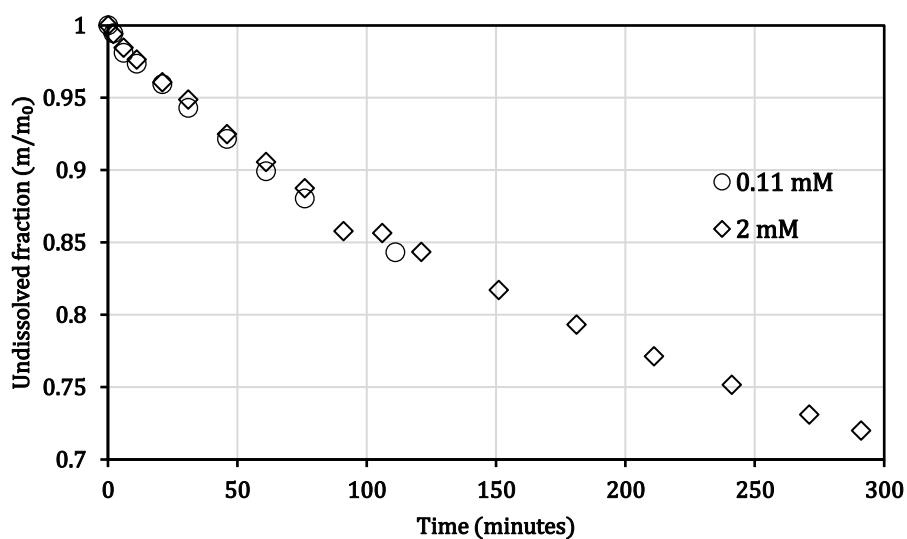

Figure 9: Initial reductive dissolution tests using varying material concentrations from WMLB, where T = 25°C, and LAH2 = 10 mM. Later measurements indicated that at $t = 4103$ $m/m_0 = 0.40$, and at $t = 1256$ $m/m_0 = 0.53$ for 0.11 mM and 2 mM, respectively.

Until a reaction time of around 60 minutes the relative Fe(II) concentrations varied by less than 1% (*Figure 9*). This implies that the iron-oxide dissolution rates were approximately independent of the LAH2 concentration. Furthermore, measurements at the final time-points indicate the reaction took nearly three days to reach approximately 60% completion. Given the time-constraints and the nature of the fitting equations, it is vital for the reaction to reach near-completion, as there it will usually express asymptotic behaviour. Henceforth, the choice was made to elevate the operating temperature to 60°C as a means to increase the reaction rate. This approach successfully reduced the experiment run-time to below approximately five hours and allowed for the majority of samples to reach near completion, as will be shown in section *4.3.3. Ferrozine data and parameter fitting*.

4.3.2 Fe(II) production and H⁺ consumption

The following section contains a demonstration of the evolution of Fe(II) concentrations from ferrozine and titration data over time. An explanation of how the H^+ consumption data was calculated and transformed into Fe(II) concentrations is provided in *Appendix D*. The stoichiometry of *Equation 14* was applied to the dissolution and pH data to evaluate whether other materials in the iron-containing by-products have had any effect on the evolution of the titration data.
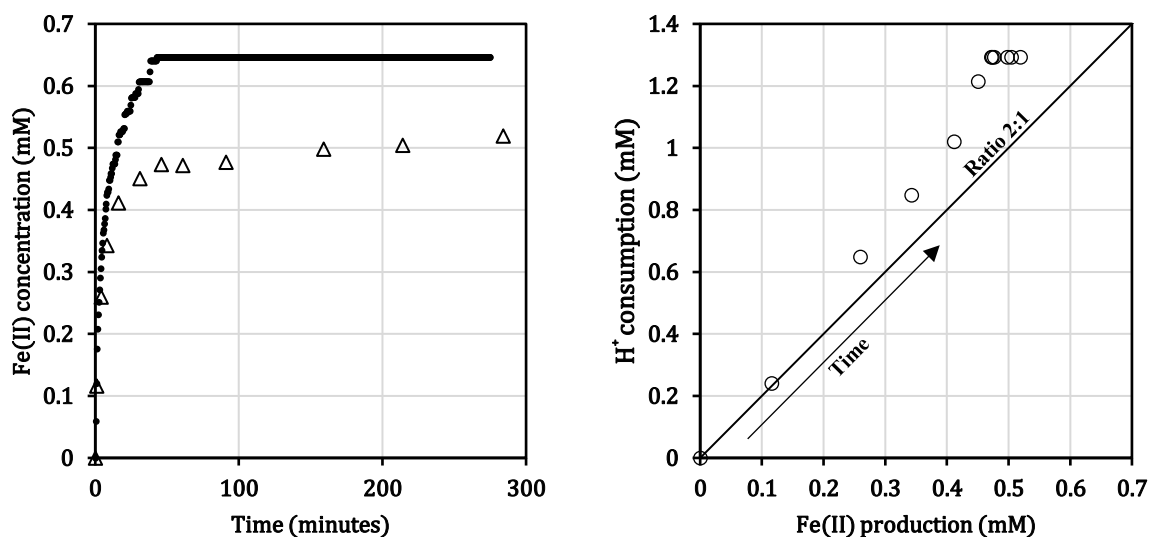

Figure 10: Calculated Fe(II) concentrations from H^+ consumption data (•) and measured Fe(II) production from ferrozine data (Δ) over time (left) and the H^+ consumption from titration data versus the Fe(II) concentration from ferrozine data (O) together with the stoichiometric ratio expected between H^+ and Fe(II) (right). T = 60°C, mat. = 1 mM (assuming all FeOOH), and LAH2 = 10 mM. The data belongs to sample VITVEE.

The ferrozine data from *Figure 10* indicates a fast initial dissolution rate, after which the reaction slows down significantly and continues gradually (Larsen and Postma, 2001; Larsen et al., 2006; Postma, 1993). The H^+ consumption, on the other hand, shows a rapid dissolution, and reaches completion in approximately 45 minutes. Evidently, the H^+ consumption was in excess of the Fe(II) production. This means that there were other species in the suspension that caused increases in pH, such as the dissolution of carbonates.
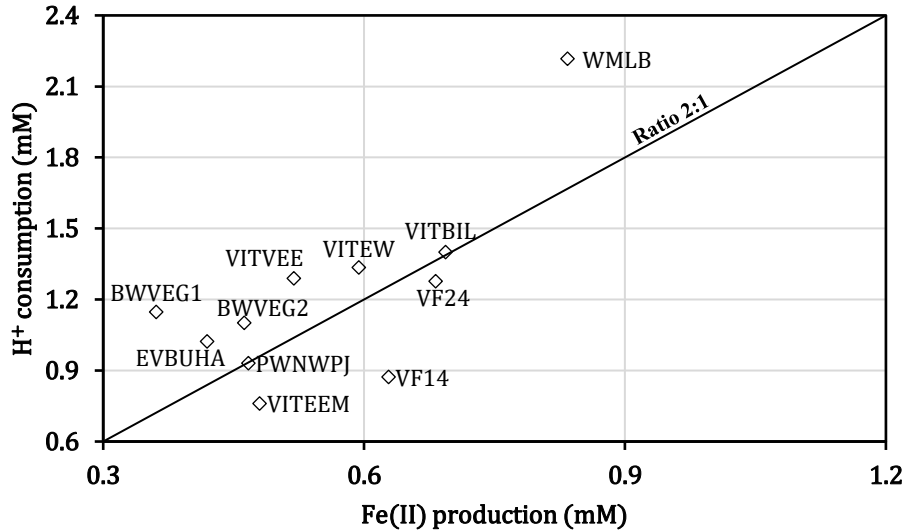
Figure 11: H$^+$ consumption data versus the Fe(II) concentrations from ferrozine data for each sample at the respective $t_{fin, ferrozine}$ time-points, where T = 60°C, mat. = 1 mM (assuming all Fe-OOH), and LAH2 = 10 mM. The stoichiometric ratio expected between H$^+$ and Fe(II) is represented by the solid line. Data for EVHUI was not included in this graph due to H$^+$ consumption data corruption.

Most H$^+$ consumption evolutions either over- or underestimated the Fe(II) reduction that was expected as per the 2:1 ratio (*Figure 11*). The data of H$^+$ and Fe(II) generally increasingly deviate from the expected stoichiometry with time. Therefore, the H$^+$ consumption data cannot be used as a continuous measurement of the reaction progress, and instead, the ferrozine data was favoured. Interestingly, the H$^+$ consumption data for BWVEG1 and WMLB showed the largest discrepancies from the expected stoichiometry, which according to their X-Ray diffractograms are dominated by calcite.

4.3.3. Ferrozine data and parameter fitting

Prior to data fitting, the raw Fe(II) data was evaluated and compared. In this section, the Fe(II) evolution of all samples are categorised. The results indicate the materials generally have a fast reacting first phase, after which the reaction slows down significantly into a near-linear second phase over time (*Figure 12*).
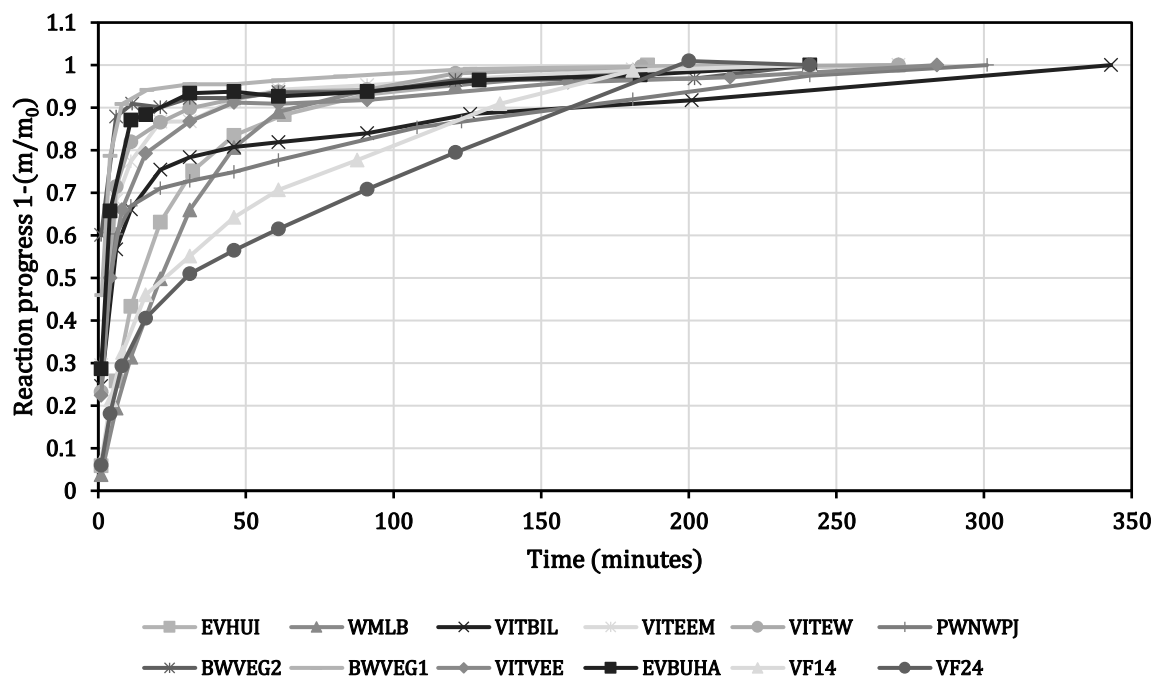

Figure 12: Fe(II) evolution data over time of all iron-containing by-product samples expressed as the dissolved fraction of the final time-point Fe(II) concentration data, hence the value of the reaction progress will always be 1 at the last time-point.

The data indicates there are sets of similarities between the reaction profiles, which allows for the samples to be sorted by type. In these classifications the main considerations were the slope and relative portion of the primary and secondary phase (*Figure 12*). Or, in cases where the profiles did not follow this basic structure, the absence thereof. This led to a total of four categories, with the following classifications presented in *Table 3*.

Table 3: Samples categorised by reactive behaviour.

Cat. I	Cat. II	Cat. III	Cat. IV
Reaction nearly complete after highly reactive primary phase, small Fe(II) contribution from secondary phase	Highly reactive primary phase, and substantial Fe(II) contribution from secondary phase	Gradual single phase throughout the entire reaction	Approximately half of Fe(II) from primary phase, another half from secondary phase
BWVEG1 BWVEG2 EVBUHA VITEEM VITEW VITVEE	PWNWPJ* VITBIL*	EVHUI WMLB	VF14 VF24

Categories are decreasingly reactive from left to right. * Has not reached completion

When the classifications were combined with their respective X-Ray diffractograms, a couple of interesting observations arose. Cat. I, the most reactive, only has materials that contain 2-line Fh, whilst Cat. IV, the least reactive, only has materials that contain 6-line Fh and goethite. Cat. II and Cat. III materials, individually, show similar reactive behaviour, although they contain different iron-oxides. This indicates that one cannot always expect similar reactive behaviour for XRD-similar materials. However, in general, the data do suggest 2-line Fh containing materials to be more reactive than 6-line Fh and goethite containing materials.

The m/m_0 data resulting from applying the transformations to the raw Fe(II) data from fitted according to the methods described in *3.4 Data-fitting procedure* (*Figure 13*).
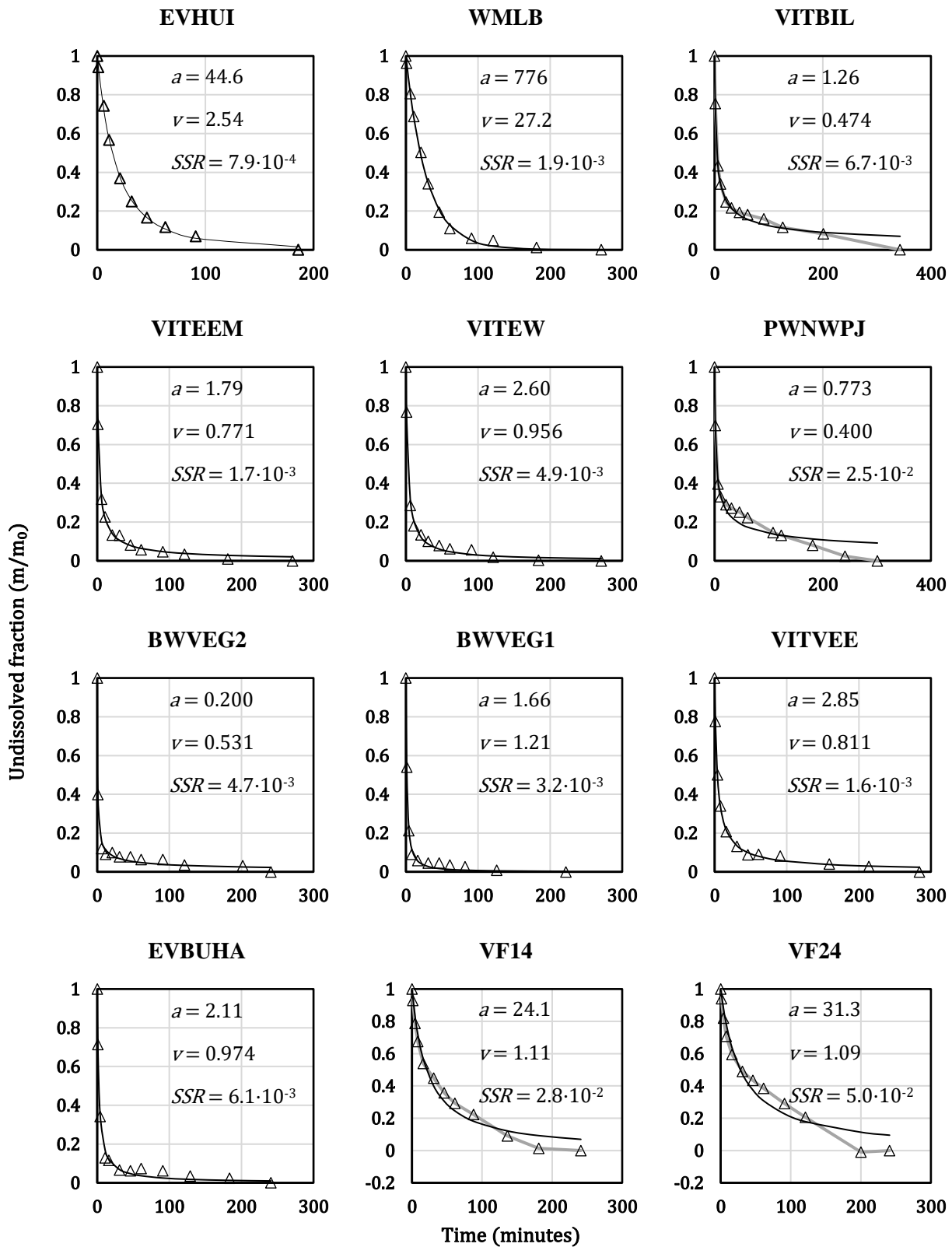
Figure 13: dissolution data (Δ) and data fits (solid lines) of all 12 iron-containing by-product samples at $T = 60°C$, *mat. < 1 mM*, and *LAH2 = 10 mM*; data fitting was performed using the Solver function in Excel with a Sum of Square Residuals (SSR) method on equation (*8*) which provides the fitting parameters *a* and *v* , m/m_0 values at $t = 0$ are assumed to be 1. In some cases, real data points were linearly connected.

In the majority of cases the parameter fitting procedure supplies good fits. However, for samples PWNWPJ, VITBIL, VF14, and VF24 there is an obvious misfit, where the fitted function increasingly diverges from the data with time. When considering the real-time data, for VITBIL and PWNWPJ, this may be explained by the reaction consisting of two distinct phases, causing the fit not adhering to the data. In addition, these reactions have not reached completion, which may be a requirement to perform proper fitting. For VF14 and VF24, the problem is, thus, slightly different as these reactions have reached completion, but do not conform to the curvature that the fitting function requires. Instead, they express three distinct linear sections, which the fitting function has trouble accommodating for. However, the goal of this study is not to attempt to improve the models used to explain the data. Although the fit may not always be appropriate, this fact will be taken into consideration in the discussion. The fitting functions provided parameters a and v, which were used to calculate k_{app} and γ_{app}. These values allowed for further, more refined, categorisation of the iron-containing by-products.

Table 4: free parameters a and v used to calculate the apparent rate constant (k_{app}) and apparent reactivity (γ_{app}) of the iron-oxides in the iron-containing by-product samples using *Equation 11* and *Equation 12* to produce rate laws of the general form of *Equation 13*: $J/m_0=\mathbf{k_{app}}(m/m_0)^{\wedge}\mathbf{\gamma_{app}}$. The samples are ordered from highest to lowest initial reaction rate, i.e. k_{app}.

Initialism	a	v	k_{app}	γ_{app}	$t_{1/2}$	Reducible Fe(II) fraction
	[-]	[-]	[min^{-1}]	[-]	[min]	[-]
BWVEG2	0.200	0.531	2.7	2.9	0.54	0.32
BWVEG1	1.66	1.21	$7.3 \cdot 10^{-1}$	1.8	1.3	0.23
PWNWPJ	0.773	0.400	$5.2 \cdot 10^{-1}$	3.5	3.6	0.31
EVBUHA	2.11	0.975	$4.6 \cdot 10^{-1}$	2.0	2.2	0.27
VITEEM	1.79	0.771	$4.3 \cdot 10^{-1}$	2.3	2.6	0.31
VITBIL	1.26	0.474	$3.8 \cdot 10^{-1}$	3.1	4.2	0.45
VITEW	2.60	0.956	$3.7 \cdot 10^{-1}$	2.0	2.8	0.39
VITVEE	2.85	0.812	$2.8 \cdot 10^{-1}$	2.2	3.9	0.34
EVHUI	44.6	2.54	$5.7 \cdot 10^{-2}$	1.4	14	0.44
VF14	24.1	1.11	$4.6 \cdot 10^{-2}$	1.9	21	0.39
WMLB	776	27.2	$3.5 \cdot 10^{-2}$	1.0	20	0.54
VF24	31.3	1.09	$3.5 \cdot 10^{-2}$	1.9	28	0.44

$\gamma_{app} \rightarrow 1$ means the assemblage of iron-oxides is generally more homogeneous; the relatively larger the k_{app} value, the higher the initial reaction rate is. The reducible Fe(II) fraction represents the Fe(II) mass extracted at the final measuring time-point divided by the mass of injected iron-containing by-product.

The data indicates the apparent rate constant k_{app} may vary by two orders of magnitude, and the reactivity γ_{app} ranges between 1.0 and 3.5 (*Table 4*). This implies there can be significant differences in the overall reactivities and iron-oxide heterogeneities between samples. Interestingly, iron-containing by-products that have apparently similar compositions based on X-Ray diffractograms can express varying γ_{app} values, which implies individual minerals can range in heterogeneity and thus reactivity. Nevertheless, the γ_{app} values appear to increase as the general material diversity gets larger, as per the number of peaks on the X-Ray diffractograms. Diffractograms dominated by calcite and 2-line Fh tend to have higher k_{app} values than those dominated by just 2-line Fh. Those dominated by 6-line Fh and goethite generally have rate constants an order of magnitude lower than those containing 2-line Fh. Although no correlation was found between k_{app} and γ_{app} values, there may be a correlation significant enough to affect the calculated model values between the parameters a and v. This suggests the model from Postma (1993) could provide many different solutions for a and v for individual samples. In principle this means that a single data set could be explained by the fitting function using a range of k_{app} and γ_{app} values. However, a sensitivity analysis performed using the data from VITEEM showed that, with a variety of initial values for a and v, the calculated k_{app} and γ_{app} values changed insignificantly (*Appendix C*).

5. Discussion

The XRD results from micronised iron-containing by-products can be confidently used to determine their mineral composition. The data indicate that although all materials contain amorphous ferrihydrites, quartz and calcite, there can be significant differences between iron-containing by-products and can be classified into one of three categories accordingly: (1) 2-line Fh/calcite, (2) 2-line Fh, and (3) 6-line Fh/goethite. Wołowiec et al. (2019) showed that a typical XRD pattern for iron-containing by-products to consist of amorphous Fe-oxides, calcite, and quartz. Finlay et al. (2021) found similar results, with the addition of goethite. Although raw XRD data on iron-containing water treatment residuals to our knowledge appeared scarce, it stood out that neither the presence of 6-line Fh, nor excess calcite were determined by others. However, this may be explained by the iron-containing by-products stemming from processes where precipitative lime-softening has been applied, which causes the precipitation of $CaCO_3$. According to the USEPA (2011) this process is often combined with filtration; therefore, it is possible that the iron-containing by-product and $CaCO_3$ product ended up mixed. In addition, it is interesting that 6-line Fh and goethite were always paired. In principle, the formation of goethite can come from the Ostwald-like ripening of ferrihydrites, where they dissolve and goethite precipitates. Usually, this takes place between pH 2-5 and 10-14 (Cudennec and Lecerf, 2006). Kukkadapu (2003) showed that 2-line Fh transitions to more crystalline products 6-line Fh, and eventually goethite over time. Although it is curious that 6-line Fh was not separately found in any iron-containing by-products it may be the case that the time-window for only 6-line Fh to be present is very small in water treatment residuals or that the conditions promote 6-line Fh and goethite formation to take place at the same time.

Finally, the presence of vivianite and baricite in sample VITVEE and siderite and oligonite in PWNWPJ were unexpected. For VITVEE this would either suggest there was ample phosphate present in the groundwater or may be an indication of phosphate dosing (Goedhart, 2021). However, through personal communication with Tonnie Hemme (Aquaminerals, 2021) we know the drinking water treatment company reported not to have used phosphate dosing at this location, nor were the groundwater phosphate concentrations elevated at the time. Therefore, it is not possible to ascertain why these materials were present. On the other hand, the presence of oligonite and siderite in PWNWPJ might be explained by the raw water stemming from surface water. This usually contains high OM concentrations and may be high in carbonates, reportedly the raw water is alkalized before the flocculants $Fe(III)_2(SO_4)_3$ and $Fe(III)Cl_3$ are added. It could be that these alkaline conditions promote the formation of various carbonate minerals similar to precipitative lime-softening (USEPA, 2011). However, it is not clear what the specific conditions were; thus, it is not possible to say for certain why oligonite and siderite have formed.

In order to resolve these knowledge gaps, it would be valuable to get process condition data of all iron-containing by-products, as these may aid in explaining the visible trends as well as the outliers. Higher confidence in determination of types of iron-oxide minerals in the X-Ray diffractograms may be achieved by more refined data fitting and the use of additional instrumental analyses such as EXAFS and Raman spectroscopy. This could also elucidate whether there have been any effects of high calcium contents, signified by the dominance of calcite in X-Ray diffractograms, on iron-oxide crystallinity and thus stability. Mos et al. (2018) also determined that better readings can be obtained by using a Co cathode instead of a Cu cathode when investigating iron-containing materials, as much of the nuance can be lost due to higher backgrounds from Fe X-Ray fluorescence. Perhaps it would be valuable to consider using cobalt radiation in the continuation of iron-containing by-product characterisation.

Although the DTG data showed variations in peak positions and intensities, the overall structures between materials were very similar. According to the X-Ray Diffractograms, all iron-containing by-products combined principally consist of calcite, Fh, and goethite, thus TGA and DTG data from other sources concerning these minerals were compared to the data in this paper. Sources have found varying DTG peak ranges for ferrihydrites and goethite. Pieczara et al. (2020) reported the loss of surface water

from ferrihydrite to have a maximum at 130°C. Michel et al. (2010) on the other hand have found the loss of adsorbed water to take place below 125°C, whilst dehydroxylation reactions were observed above that temperature. Although this does not provide a clear answer, it suggests the initial peak between 27-105°C seen in the thermograms of *Figure 4* belong to Fh. This implies the presence of Fh in all samples, which is in line with the findings from XRD. Despite this information not specifying the type of Fh, it is useful to have a two-fold verification of its general presence. King et al. (2015) also show a small peak belonging to Fh dehydroxylation that occurs at approximately 240°C. This could indicate the initial peak of the doublets visible in *Figure 4* belong to the dehydroxylation of ferrihydrite. The phase transition of Fh to hematite should be visible at 460°C, but only manifests as an exotherm in Differential Thermal Analysis, of which no data is available (Equation 16; Pieczara et al., 2020),

$$2Fe_5HO_8 \cdot 4H_2O \rightarrow 5Fe_2O_3 + 5H_2O \qquad (16)$$
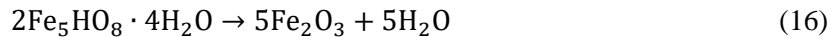
Furthermore, Pérez-Maqueda et al. (2000) reported the loss of surface water of various gradations of ground goethite to take place between 40-170°C, and two consecutive goethite dehydroxylation reactions between 170-300°C and 300-370°C, producing in total three peaks of consecutively increasing intensity. Gualtieri and Venturelli (1999) found a doublet with a first peak at 255°C and a second at 282°C. Ford and Bertsch (1999) determined the goethite-hematite phase transition, otherwise known as the bulk dehydroxylation, to take place at approximately 270°C. They also determined there were three dehydroxylation/dehydration reactions prior to the goethite-hematite phase transition, which cause relatively low intensity broad peaks. The transition of goethite to hematite should be visible in DTG graphs (Equation 17.; Gialanella et al., 2010). Despite goethite's known presence in a number of samples from XRD, this transition peak at 270°C was not visible in those data.

$$2FeOOH \rightarrow Fe_2O_3 + H_2O \qquad (17)$$

Interestingly, the DTG data in *Figure 4* follow the reported basic structures, thus implying there are stages of surface water loss and dehydroxylation in these samples. However, the supposed dehydroxylation peaks occur at lower temperatures than expected, in the range between 185-205°C and 230-250°C. Perhaps the goethite is poorly crystalline, meaning both the dehydroxylation and bulk structurally bound H_2O require less energy input to be removed, which may explain the peak shift to lower temperatures. However, this would suggest the presence of goethite in samples, where we did not expect it. Unfortunately, information concerning the dehydroxylation reactions of ferrihydrites was scarce, which made it difficult to discern whether these peaks may have belonged to a different group of iron-oxides.

Therefore, we will assume the initial broad peak belongs to iron-oxide water loss, whilst the following sharper peaks are a result of iron-oxide dehydroxylation reactions. However, with the available data it is not fully possible to assign those DTG peaks to specific minerals. The DTG curves are seemingly incomplete without complementary DTA curves. DTA can show exotherms and endotherms indicating phase transitions such as those of ferrihydrite-hematite and goethite-hematite more explicitly. It would be valuable for the iron-containing by-products to be analysed using this technique, to assert which materials contain ferrihydrites and goethite and verify the interpretation of the X-Ray diffractograms. Specifically, the DTG and DTA curves of synthetic ferrihydrites and synthetic goethite could be used to help identify characteristic iron-containing by-product peaks.

Although data fitting procedures were generally successful, four sample fits (VITBIL, PWNWPJ, VF14, and VF24) diverged from the real-time measurements rather quickly. All misfit iron-containing by-products had in common that their real-time data consisted clearly of a distinct first phase, and a distinct second phase with a sharp transition between them. Perhaps the kinetic model is only able to account for transitions like this when they are more gradual, and thus more representative of the reactive continuum that it is supposed to adhere to. This brings an interesting point to the surface, which is that

the lack of a slow and gradual transition of one phase to another must imply that these iron-containing by-products mostly consist of two starkly different mineral phases.

Nevertheless, the reductive dissolution data indicate that there were significant differences in the reactivity of iron-containing by-products from various sources and could largely be described by fitting Fe(II) time-evolution data to a general rate-law for polydisperse suspensions of the form $J/m_0=k_{app}(m/m_0)^{\gamma_{app}}$. This means their reactivities could be quantitatively compared by plotting the linear relationship of $-log(J/m_0)$ versus $-log(m/m_0)$, which provided initial reaction rates $(-log(m/m_0)=0$, then $k_{initial}=k_{app})$, terminal reaction rates $(-log(m/m_0)=0$, then $k_{terminal}=10^{-(k_{app}+\gamma_{app})})$, and iron-oxide reactivities/heterogeneities γ_{app} (slope).
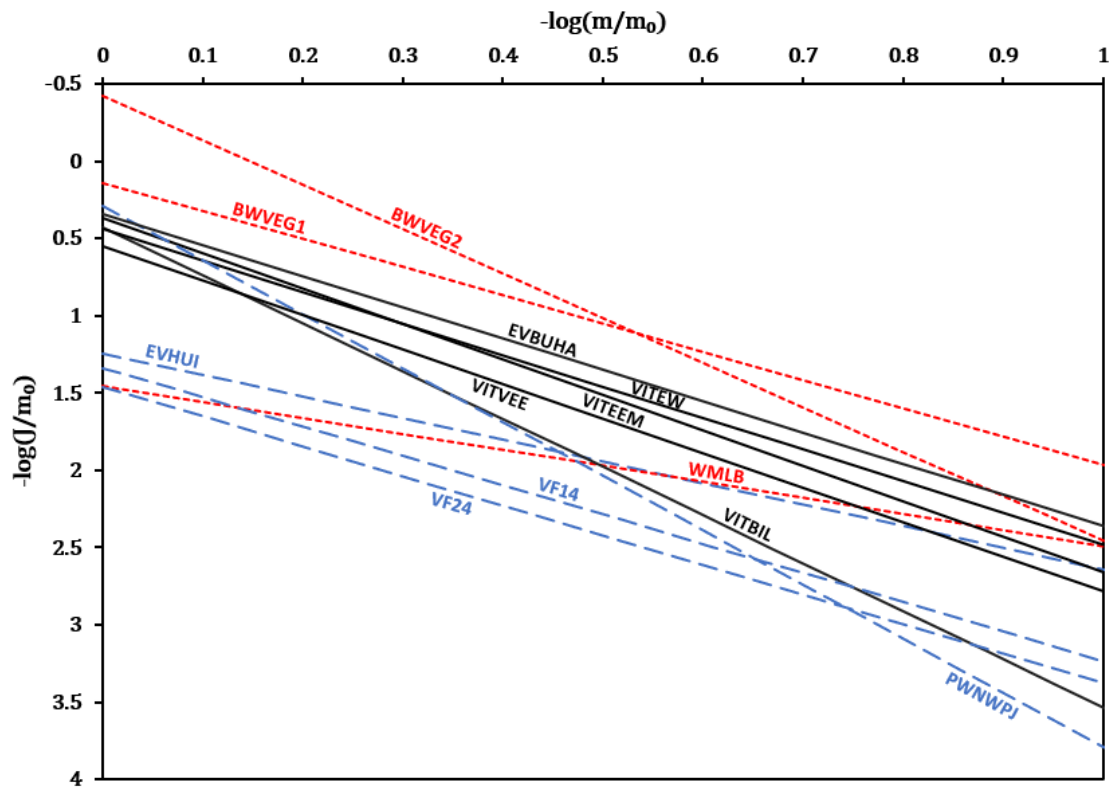

Figure 14: Reductive dissolution of all iron-containing by-product samples where $-log(m/m_0)$ represents the undissolved fraction of material, 0 is the start and 1 the end of the reaction on the x-axis. The $-log(J/m_0)$ on the y-axis represents the normalised reaction rate in orders of magnitude, thus increasing numbers imply a lower reaction rate. Various colours represent the material composition from XRD observations: (•••) Calcite/2-line Fh; (—) 2-line Fh; and (− −) 6-line Fh/goethite. $T = 60°C$, $m_0 < 1\ mM\ Fe(II)$, and $LAH2 = 10\ mM$

The data indicates there exists a strong correlation between the rates of Fe(II) production, and the dominant minerals in the X-Ray diffractograms (*Figure 14*). This is indicative of the variations in mineralogy and their control on the reductive dissolution capacities of the iron-containing by-products. Although there was sometimes overlap in reactive behaviour between different mineral compositions, the X-Ray diffractograms can evidently be used to qualitatively describe the reactivity of a sample. The data generally suggests the following order of most to least reactive, based on their k_{app} and γ_{app} values: *2-line Fh/calcite > 2-line Fh > 6-line Fh/goethite*. Our findings are both qualitatively and quantitatively in line with previously found reactivities from Larsen and Postma (2001). In addition, this study has determined there can be a significant effect on iron-oxide reactivity from calcium, which is signified by the dominance of calcite in respective X-Ray diffractograms. Although the normalisation using m_0 is usually done by looking at the oxalate or dithionite extractable iron separate from the reductive dissolution experiments, our data suggests the last-measured concentration of Fe(II) may also be used as a normalisation value. The downside, however, is that prior to the experiments it will not be known how much Fe(II) could potentially be extracted, which complicates inferring when the reaction will

have reached completion. Yet, in principle it should not make a difference in the data analysis, provided the reaction has reached completion.

Mixtures of 6-line Fh and goethite were expected to exhibit larger γ values in comparison to only 2-line Fh containing materials, as these should contain a more heterogeneous iron-pool. Interestingly, this was not the case, which implies the variability of 2-line Fh reactivity can be larger than the difference between 6-line Fh and goethite. This suggests 2-line Fh can consist of a very heterogeneous iron-pool, despite the X-Ray diffractogram indicating the presence of a singular material. Similar samples in terms of composition had similar initial reaction rates. However, the data indicates their terminal dissolution rates varied depending on the portion of goethite (EVHUI $\gamma = 1.4$ and PWNWPJ $\gamma = 3.5$) or may vary even though they principally consist of 2-line Fh (VITBIL $\gamma = 3.1$). Likewise, Larsen and Postma (2001) found a relatively large γ value of 2.3 for ferrihydrites, they argued this may be explained by the conception that ferrihydrites are indeed multi-phase heterogeneous minerals. Drits et al. (1993) proposed that ferrihydrites consist of three separate phases, which range from a more defective and thus amorphous ferrihydrite structure, all the way to nano-crystalline hematite. Essentially, where in X-Ray diffractograms a single phase of 2-line Fh was determined to be present, it may in practise contain three phases of varying proportions. This suggests that the terminal dissolution rate is controlled by the portion of the most crystalline material in an assemblage of iron-oxides, which is usually accompanied by a larger γ value indicating a rapid decrease in iron-oxide reactivity over time.

If it is assumed that the least crystalline, most defective phases, of 2-line and 6-line Fh control the initial reaction rates, it would be expected that XRD-similar materials produce similar initial reaction rates. This is generally true, which implies that materials where 6-line Fh was determined to be present do not contain any 2-line Fh. Two exceptions to this are WMLB and PWNWPJ, which were thought to contain only 2-line Fh and 6-line Fh, respectively. Interestingly, WMLB expresses an initial dissolution rate similar to 6-line Fh containing materials, whilst PWNWPJ expresses rates similar to 2-line Fh containing materials. This would imply that these samples actually contained different ferrihydrites than were observed in their X-Ray diffractograms. Perhaps these materials have been wrongly determined, which may indicate the need of a more robust approach for ferrihydrite type determination. However, it is possible that the presence of siderite in PWNWPJ has contributed to the Fe(II) evolution, as siderite is easily dissolved under acidic conditions (Golubev et al., 2009).

Ignoring WMLB, the data also suggests that materials with X-Ray diffractograms dominated by calcite (BWVEG1 and BWVEG2) can have significantly higher initial reaction rates than other materials. However, this was only observed for two materials that both originated from the same drinking water treatment plant. Nevertheless, if it is assumed that the initial reaction rate is controlled by the least crystalline phase of 2-line Fh, then initial reaction rates similar to other 2-line Fh containing materials would be expected. Given this is not completely true, it is possible that the presence of calcium has had a significant effect on the reactivity, and thus on the 2-line Fh defectiveness. This implies that, not only can 2-line Fh consist of multiple iron-oxide phases ranging in crystallinity, the most defective phase may become forcibly more defective in the presence of Ca^{2+}. This may be explained by the formation of Ca-Fe-P minerals that can form when varying concentrations of the individual constituents are present in solution prior to oxidation (Senn et al., 2015 and Voegelin et al., 2010). Interestingly, this was not observed for WMLB. If the assumption is made that this sample consists only of 6-line Fh, then the presence of calcium appears to have had no effect on the defectiveness of the least crystalline phase of 6-line Fh. Another explanation may simply be the release of Fe(II) from carbonate dissolution. Regardless of the mechanism, materials with X-Ray diffractograms dominated by calcite can be more reactive than those that do not.

If the initial and terminal reaction rates are controlled by the least and most crystalline materials respectively, then the reactivity of individual phases can be ordered from most to least reactive as follows: *Ca-defected 2-line Fh > 2-line Fh > 6-line Fh > goethite*, with the addition that some of the

more crystalline phases of ferrihydrite may be less reactive than goethite. When $m/m_0 = 1$, the initial reaction rate $J/m_0 = k_{app}$, which provides initial reaction rates for the least crystalline phases to adhere to *Table 5*.

Table 5: Fitted initial reaction rate ranges J/m_0 belonging to Ca-defected 2-line Fh, 2-line Fh, and 6-line Fh, this excludes WMLB $3.5 \cdot 10^{-2}$ min^{-1} and PWNWPJ $5.2 \cdot 10^{-1}$ min^{-1} under the assumption that their XRD determinations were wrongly assigned. $T = 60°C$ and $LAH2 = 10\ mM$.

Ca 2-line Fh [min^{-1}]	*2-line Fh* [min^{-1}]	*6-line Fh* [min^{-1}]
$7.29 \cdot 10^{-1} - 2.66 \cdot 10^{-1}$	$2.84 \cdot 10^{-1} - 4.61 \cdot 10^{-1}$	$3.48 \cdot 10^{-2} - 5.68 \cdot 10^{-2}$

Since reaction constants rapidly increase at elevated temperatures, reaction rates determined in this study at 60°C are not directly comparable with those determined for synthetic iron-oxides found by Larsen and Postma (2001) at 25°C. However, a brief back-of-the-envelope calculation with a rewritten Arrhenius equation of the form $k(T_2)=k(T_1)e^{\wedge}((E_a/R)(1/T_1-1/T_2))$ was performed (*Appendix E*). Activation energies (E_a) reported by Yee et al. (2006) for the crystallisation of 2-line Fh to goethite, which requires ferrihydrite dissolution as an intermediate step, and E_a found by Erbs et al. (2008) for the reductive dissolution of 6-line Fh were used in these calculations (Table 6).

Table 6: rate constants of this study and Larsen and Postma (2001) compared at $T = 25°C$, this does not contain Ca-dominated 2-line Fh rate constants.

	k_{2-fh} [s^{-1}]	k_{6-fh} [s^{-1}]
This study	$4.4 - 7.2 \cdot 10^{-4}$*	$4.6 - 7.4 \cdot 10^{-5}$†
Larsen and Postma (2001)	$6.6 - 7.6 \cdot 10^{-4}$	$7.4 \cdot 10^{-5}$

* transformed using $E_a = 56\ kJ/mol$ for 2-line Fh from Yee et al. (2006)
†transformed using a nearing value $E_a = 60\ kJ/mol$ for 6-line Fh from Erbs et al. (2008)

Evidently, rate constants found in this paper were very similar to those reported by Larsen and Postma (2001). This further strengthens the argument that the initial reaction rates are controlled by the most reactive material observed in the X-Ray diffractograms, and that these are 2-line Fh and 6-line Fh. Similarly, if we assume WMLB contains 6-line Fh and PWNWPJ contains 2-line Fh, then rate constant transformations of the same nature as previously performed provide $k_{WMLB} = 4.59 \cdot 10^{-5}\ s^{-1}$, and $k_{PWNWPJ} = 8.1 \cdot 10^{-4}\ s^{-1}$, which again are near rate constants observed by Larsen and Postma (2001) for the respective mineral phases. Combined with the knowledge that the most reactive material controls the reaction rate; this strongly implies these materials were mischaracterized with XRD.

However, in order to get an idea of reactivity in specific environments, such as soils, sediments, or waste-water; a transfer function needs to be applied, where a linear-free energy relationship (LFER) is assumed. For example, Bonneville et al. (2009) determined bacterial reduction rates of iron-oxides to have an LFER with their respective solubility products. As they had previously established (Bonneville et al., 2004) that the solubility controls the reactivity in both the abiotic and enzymatic reduction of iron-oxides. However, Hyacinthe et al. (2006) emphasize that there are parallels between abiotic and microbial reductive dissolution, there exist intrinsic differences between them. Perhaps using common iron reducing bacteria from these environments, similar relations can be established with the iron-containing by-products from this study.

Nevertheless, some comments can be made on potential uses for the various types of iron-containing by-products based on their reactivity and their contents. For example, those that contain goethite may be better used in the immobilisation of sediment P. Goethite usually has a high specific surface area and

is less reactive than ferrihydrites, which promotes P immobilisation through sorption whilst having a slower reductive dissolution rate. However, materials consisting mainly of ferrihydrite can also be used if the objective is rapid reductive dissolution and consequent Fe-P mineral precipitation. In any case, the residency time of iron in sediment is controlled by redox processes and upwelling (Busigny et al., 2016), so the desired time of reactivity can be decided on depending on the purpose. Elliott et al. (2002) found that hematite (alpha-Fe2O3) has a significantly lower P immobilisation capacity than amorphous iron-oxides. They also found that calcium-containing by-products can immobilise P through Ca-P mineralisation. Therefore, those iron-containing by-products dominated by calcite are perhaps desirable for use in agricultural soils with a potentially mobile P fraction. In waste-water treatment, the low hydraulic retention time in comparison to the complete iron-oxide dissolution time implies a need for materials that can react very fast. Therefore, it is probably sufficient to use 2-line Fh containing iron-containing by-products that also express low γ values to obtain maximum reactivity. In addition, iron-containing by-products containing significant portions of calcite appear to have much higher reaction rates and may, thus, also prove a desirable source of iron-containing by-products for waste-water treatment.

6. Conclusion

This study has successfully demonstrated the application of a general rate-law for polydisperse suspensions of the form $J/m_0=k_{app}(m/m_0)^{\gamma_{app}}$ to Fe(II) reductive dissolution data from various drinking water treatment residuals. Although the data-set of twelve samples was relatively small, clear trends in terms of reactive behaviour could be determined. Generally, the model produced consistent results for XRD-similar materials, where the assemblage reactivity in decreasing order was found to be *2-line Fh/calcite > 2-line Fh > 6-line Fh/goethite*. Materials with more diverse X-Ray diffractograms were also found to have higher γ_{app} values, thus being indicative of a more heterogeneous Fe(II) pool. It was possible to isolate the effects of individual phases on initial and terminal dissolution rates. This led to the reactivity of the phases from most to least reactive accordingly: *Ca-defected 2-line Fh > 2-line Fh > 6-line Fh > goethite*, where the least crystalline phase in an assemblage controls the initial dissolution rate, and the most crystalline phase controls the terminal dissolution rate. Apparent rate constants for 2-line and 6-line Fh, transformed by the Arrhenius equation, were determined to be $k_{2\text{-}Fh} = 4.41 - 7.16 \cdot 10^{-4}\ s^{-1}$ and $k_{6\text{-}Fh} = 4.56 - 7.44 \cdot 10^{-5}\ s^{-1}$, which is in line with findings from Larsen and Postma (2001). This means X-Ray diffractograms can generally be consulted to obtain a qualitative impression of the relative reactivities of iron-containing by-products.

However, due to the nature of ferrihydrites and the presence of other crystalline materials, it can sometimes be arduous to discern whether the X-Ray diffractograms showed a characteristic 2-line or 6-line Fh structure. This could complicate setting expectations of initial reactivity. In addition, it is thought that ferrihydrite can consist of three distinct phases (Drits et al., 1993). The least reactive of these is nano-crystalline hematite, which Larsen and Postma (2001) suggest may control the terminal dissolution rate, and if assumed present, our data indicate nano-crystalline hematite may be less reactive than goethite. Similarly, results from this study show goethite also has the capability to control the terminal dissolution rate. Samples PWNWPJ and WMLB expressed rate constants similar to 2-line Fh and 6-line Fh, although determination by XRD did not indicate these materials were present. Therefore, a robust approach for the determination of 2-line and 6-line Fh in XRD is necessary to verify the which ferrihydrite is present. This may aid predictions of overall reactive behaviour. In conjunction, more research is needed to determine the proportion of the various ferrihydrite phases, as these can significantly affect the overall reactivity.

Similarly, the data suggests there is a significant effect of calcium on the relative defectiveness of the initial phase of 2-line Fh, but not on the initial phase of 6-line Fh. Yet, our data on this is scarce, and it was not possible to determine the precise extent, if any at all, of the effect of calcium. Senn et al. (2015) and Voegelin et al. (2010) showed that Ca and P affect iron-oxide precipitation. It would be valuable to produce a range of synthetic ferrihydrites with various Ca-P-doping ratios and to apply the methods within this paper to elucidate how Ca-P may affect the reductive dissolution capacities of the produced iron-oxides. Materials with very high reactivities may be desirable for applications with low effluent residency times (such as waste-water treatment), and Ca-containing by-products can be effective for P immobilisation in soil, which means Ca-dominated ferrihydrites in iron-containing by-products could prove suitable candidates for these purposes.

Nevertheless, the reductive dissolution data and kinetic model can successfully describe the reactivities of all iron-containing by-products and can even be translated to be compared to other research. Perhaps it is possible to take this data and translate it to various applications, such as sediments, soils, and waste-water treatment, by use of a transfer function when assuming a linear free energy relationship. This would unlock the potential of reductive dissolution experiments in the laboratory to be descriptive of processes in nature and industry without the constant need for real-time testing. This could be useful in better understanding the role of reductive dissolution of iron-oxides in P immobilisation. However, before this can be attempted, the performed experiments should be continued with other iron-containing

by-products to further verify the applicability of the model from Postma (1993), and to further establish trends in reactive properties of iron-containing by-products in relation to production process conditions.

Bibliography

Alewell, C., Ringeval, B., Ballabio, C., Robinson, D. A., Panagos, P., & Borrelli, P. (2020). Global phosphorus shortage will be aggravated by soil erosion. *Nature communications*, *11*(1), 1-12.

Bakker, E. S., Van Donk, E., & Immers, A. K. (2016). Lake restoration by in-lake iron addition: a synopsis of iron impact on aquatic organisms and shallow lake ecosystems. *Aquatic Ecology*, *50*(1), 121-135.

Bennett, E. M., Carpenter, S. R., & Caraco, N. F. (2001). Human impact on erodable phosphorus and eutrophication: a global perspective: increasing accumulation of phosphorus in soil threatens rivers, lakes, and coastal oceans with eutrophication. *BioScience*, *51*(3), 227-234.

Bonneville, S., Behrends, T., & Van Cappellen, P. (2009). Solubility and dissimilatory reduction kinetics of iron (III) oxyhydroxides: a linear free energy relationship. *Geochimica et cosmochimica acta*, *73*(18), 5273-5282.

Bonneville, S., Van Cappellen, P., & Behrends, T. (2004). Microbial reduction of iron (III) oxyhydroxides: effects of mineral solubility and availability. *Chemical Geology*, *212*(3-4), 255-268.

Boudreau, B. P., & Ruddick, B. R. (1991). On a reactive continuum representation of organic matter diagenesis. *American Journal of Science*, *291*(5), 507-538.

Brennan, R. B., Murnane, J. G., Sharpley, A. N., Herron, S., Brye, K. R., & Simmons, T. (2019). Soil phosphorus dynamics following land application of unsaturated and partially saturated red mud and water treatment residuals. *Journal of environmental management*, *248*, 109296.

Busigny, V., Jézéquel, D., Cosmidis, J., Viollier, E., Benzerara, K., Planavsky, N. J., ... & Michard, G. (2016). The iron wheel in lac Pavin: interaction with phosphorus cycle. In *Lake Pavin* (pp. 205-220). Springer, Cham.

Cao, J., Wu, Y., Zhao, J., Jin, S., Aleem, M., Zhang, Q., ... & Luo, J. (2019). Phosphorus recovery as vivianite from waste activated sludge via optimizing iron source and pH value during anaerobic fermentation. *Bioresource technology*, *293*, 122088.

Carpenter, S. R. (2008). Phosphorus control is critical to mitigating eutrophication. *Proceedings of the National Academy of Sciences*, *105*(32), 11039-11040.

Carpenter, S. R., Caraco, N. F., Correll, D. L., Howarth, R. W., Sharpley, A. N., & Smith, V. H. (1998). Nonpoint pollution of surface waters with phosphorus and nitrogen. *Ecological applications*, *8*(3), 559-568.

Chen, M., & Graedel, T. E. (2016). A half-century of global phosphorus flows, stocks, production, consumption, recycling, and environmental impacts. *Global Environmental Change*, *36*, 139-152.

Cheng, X., Chen, B., Cui, Y., Sun, D., & Wang, X. (2015). Iron (III) reduction-induced phosphate precipitation during anaerobic digestion of waste activated sludge. *Separation and Purification Technology*, *143*, 6-11.

Chong, E., Marak, K. E., Li, Y., & Freedman, M. A. (2021). Ice nucleation activity of iron oxides via immersion freezing and an examination of the high ice nucleation activity of FeO. *Physical Chemistry Chemical Physics*, *23*(5), 3565-3573.

Conley, D. J., Paerl, H. W., Howarth, R. W., Boesch, D. F., Seitzinger, S. P., Havens, K. E., ... & Likens, G. E. (2009). Controlling eutrophication: nitrogen and phosphorus. *Science*, *323*(5917), 1014-1015.

Cordell, Dana, and Stuart White. "Sustainable phosphorus measures: strategies and technologies for achieving phosphorus security." *Agronomy* 3.1 (2013): 86-116.

Cudennec, Y., & Lecerf, A. (2006). The transformation of ferrihydrite into goethite or hematite, revisited. *Journal of solid state chemistry*, *179*(3), 716-722.

De Vet, W. W. J. M., Van Genuchten, C. C. A., Van Loosdrecht, M. C. M., & Van Dijk, J. C. (2010). Water quality and treatment of river bank filtrate. *Drinking Water Engineering and Science*, *3*(1), 79-90.

Desmidt, E., Ghyselbrecht, K., Zhang, Y., Pinoy, L., Van der Bruggen, B., Verstraete, W., ... & Meesschaert, B. (2015). Global phosphorus scarcity and full-scale P-recovery techniques: a review. *Critical Reviews in Environmental Science and Technology*, *45*(4), 336-384.

Drits, V. A., Sakharov, B. A., Salyn, A. L., & Manceau, A. (1993). Structural model for ferrihydrite. *Clay Minerals*, *28*(2), 185-207.

Elliott, H. A., O'Connor, G. A., Lu, P., & Brinton, S. (2002). Influence of water treatment residuals on phosphorus solubility and leaching. *Journal of Environmental Quality*, *31*(4), 1362-1369.

Erbs, J. J., Gilbert, B., & Penn, R. L. (2008). Influence of size on reductive dissolution of six-line ferrihydrite. *The Journal of Physical Chemistry C*, *112*(32), 12127-12133.

Finlay, N. C., Peacock, C. L., Hudson-Edwards, K. A., & Johnson, K. L. (2021). Characteristics and mechanisms of Pb (II) sorption onto Fe-rich waste water treatment residue (WTR): A potential sustainable Pb immobilisation technology for soils. *Journal of Hazardous Materials*, *402*, 123433.

Gialanella, S., Girardi, F., Ischia, G., Lonardelli, I., Mattarelli, M., & Montagna, M. (2010). On the goethite to hematite phase transformation. *Journal of thermal analysis and calorimetry*, *102*(3), 867-873.

Goedhart, R. (2021) Vivianite precipitation: a novel concept to remove iron from groundwater. Technische Universiteit Delft, Delft. Accessed via: http://resolver.tudelft.nl/uuid:959073e0-81a4-43f8-b53a-72aaafbec74e

Golubev, S. V., Bénézeth, P., Schott, J., Dandurand, J. L., & Castillo, A. (2009). Siderite dissolution kinetics in acidic aqueous solutions from 25 to 100 C and 0 to 50 atm pCO2. *Chemical Geology*, *265*(1-2), 13-19.

Gualtieri, A. F., & Venturelli, P. (1999). In situ study of the goethite-hematite phase transformation by real time synchrotron powder diffraction. *American Mineralogist*, *84*(5-6), 895-904.

Hansel, C. M., Benner, S. G., Nico, P., & Fendorf, S. (2004). Structural constraints of ferric (hydr) oxides on dissimilatory iron reduction and the fate of Fe (II). *Geochimica et Cosmochimica Acta*, *68*(15), 3217-3229.

Hyacinthe, C., & Van Cappellen, P. (2004). An authigenic iron phosphate phase in estuarine sediments: composition, formation and chemical reactivity. *Marine Chemistry*, *91*(1-4), 227-251.

Hyacinthe, C., Bonneville, S., & Van Cappellen, P. (2006). Reactive iron (III) in sediments: chemical versus microbial extractions. *Geochimica et cosmochimica acta*, *70*(16), 4166-4180.

Ippolito, J. A., Barbarick, K. A., & Elliott, H. A. (2011). Drinking water treatment residuals: a review of recent uses. *Journal of environmental quality*, *40*(1), 1-12.

Jan, J., Borovec, J., Kopáček, J., & Hejzlar, J. (2015). Assessment of phosphorus associated with Fe and Al (hydr) oxides in sediments and soils. *Journal of Soils and Sediments*, *15*(7), 1620-1629.

Kang, S. K., Choo, K. H., & Lim, K. H. (2003). Use of iron oxide particles as adsorbents to enhance phosphorus removal from secondary wastewater effluent. *Separation Science and Technology*, *38*(15), 3853-3874.

Kemmer, G., & Keller, S. (2010). Nonlinear least-squares data fitting in Excel spreadsheets. *Nature protocols*, *5*(2), 267-281.

King, A. J., Solomon, J. R., Schofield, P. F., & Russell, S. S. (2015). Characterising the CI and CI-like carbonaceous chondrites using thermogravimetric analysis and infrared spectroscopy. *Earth, Planets and Space*, *67*(1), 1-12.

Koopmans, G. F., Hiemstra, T., Vaseur, C., Chardon, W. J., Voegelin, A., & Groenenberg, J. E. (2020). Use of iron oxide nanoparticles for immobilizing phosphorus in-situ: Increase in soil reactive surface area and effect on soluble phosphorus. *Science of the Total Environment*, *711*, 135220.

Kraal, P., van Genuchten, C. M., Behrends, T., & Rose, A. L. (2019). Sorption of phosphate and silicate alters dissolution kinetics of poorly crystalline iron (oxyhydr) oxide. *Chemosphere*, *234*, 690-701.

Kukkadapu, R. K., Zachara, J. M., Fredrickson, J. K., Smith, S. C., Dohnalkova, A. C., & Russell, C. K. (2003). Transformation of 2-line ferrihydrite to 6-line ferrihydrite under oxic and anoxic conditions. *American Mineralogist*, *88*(11-12), 1903-1914.

Larsen, O., & Postma, D. (2001). Kinetics of reductive bulk dissolution of lepidocrocite, ferrihydrite, and goethite. *Geochimica et Cosmochimica Acta*, *65*(9), 1367-1379.

Larsen, O., Postma, D., & Jakobsen, R. (2006). The reactivity of iron oxides towards reductive dissolution with ascorbic acid in a shallow sandy aquifer (Rømø, Denmark). *Geochimica et Cosmochimica Acta*, *70*(19), 4827-4835.

Li, Y., Yu, S., Strong, J., & Wang, H. (2012). Are the biogeochemical cycles of carbon, nitrogen, sulfur, and phosphorus driven by the "Fe III–Fe II redox wheel" in dynamic redox environments?. *Journal of Soils and Sediments*, *12*(5), 683-693.

Linster, C. L., & Van Schaftingen, E. (2007). Vitamin C: biosynthesis, recycling and degradation in mammals. *The FEBS journal*, *274*(1), 1-22.

Liu, W., Yang, H., Ciais, P., Stamm, C., Zhao, X., Williams, J. R., ... & Schulin, R. (2018). Integrative Crop-Soil-Management Modeling to Assess Global Phosphorus Losses from Major Crop Cultivations. *Global Biogeochemical Cycles*, *32*(7), 1074-1086.

Lun, F., Liu, J., Ciais, P., Nesme, T., Chang, J., Wang, R., ... & Obersteiner, M. (2018). Global and regional phosphorus budgets in agricultural systems and their implications for phosphorus-use efficiency. *Earth System Science Data*, *10*(1), 1-18.

Makris, K. C., Harris, W. G., O'Connor, G. A., Obreza, T. A., & Elliott, H. A. (2005). Physicochemical properties related to long-term phosphorus retention by drinking-water treatment residuals. *Environmental science & technology*, *39*(11), 4280-4289.

Michel, F. M., Barrón, V., Torrent, J., Morales, M. P., Serna, C. J., Boily, J. F., ... & Brown, G. E. (2010). Ordered ferrimagnetic form of ferrihydrite reveals links among structure, composition, and magnetism. *Proceedings of the National Academy of Sciences*, *107*(7), 2787-2792.

Michel, F. M., et al. "Similarities in 2-and 6-line ferrihydrite based on pair distribution function analysis of X-ray total scattering." *Chemistry of Materials* 19.6 (2007): 1489-1496.

Mos, Y. M., Vermeulen, A. C., Buisman, C. J., & Weijma, J. (2018). X-ray diffraction of iron containing samples: the importance of a suitable configuration. *Geomicrobiology Journal*, *35*(6), 511-517.

Nehrke, G., & Van Cappellen, P. (2006). Framboidal vaterite aggregates and their transformation into calcite: a morphological study. *Journal of crystal growth*, *287*(2), 528-530.

Ngatia, L., & Taylor, R. (2018). Phosphorus eutrophication and mitigation strategies. In *Phosphorus-Recovery and Recycling*. IntechOpen.

Ngatia, L., Grace III, J. M., Moriasi, D., & Taylor, R. (2019). Nitrogen and phosphorus eutrophication in marine ecosystems. *Monitoring of marine pollution*, 1-17.

O'Connell, D. W., Jensen, M. M., Jakobsen, R., Thamdrup, B., Andersen, T. J., Kovacs, A., & Hansen, H. C. B. (2015). Vivianite formation and its role in phosphorus retention in Lake Ørn, Denmark. *Chemical geology*, *409*, 42-53.

Oey, I., Verlinde, P., Hendrickx, M., & Van Loey, A. (2006). Temperature and pressure stability of L-ascorbic acid and/or [6s] 5-methyltetrahydrofolic acid: A kinetic study. *European Food Research and Technology*, *223*(1), 71-77.

Pal, P. (2017). *Industrial water treatment process technology*. Butterworth-Heinemann.

Pérez-Maqueda, L. A., Šubrt, J., Balek, V., Criado, J. M., & Real, C. (2000). Use of emanation thermal analysis in characterisation of nanosized hematite prepared by dry grinding of goethite. *Journal of thermal analysis and calorimetry*, *60*(3), 997-1007.

Pieczara, G., Manecki, M., Rzepa, G., Borkiewicz, O., & Gaweł, A. (2020). Thermal Stability and Decomposition Products of P-Doped Ferrihydrite. *Materials*, *13*(18), 4113.

Postma, D. (1993). The reactivity of iron oxides in sediments: a kinetic approach. *Geochimica et Cosmochimica Acta*, *57*(21-22), 5027-5034.

Raiswell, R., Vu, H. P., Brinza, L., & Benning, L. G. (2010). The determination of labile Fe in ferrihydrite by ascorbic acid extraction: methodology, dissolution kinetics and loss of solubility with age and de-watering. *Chemical Geology*, *278*(1-2), 70-79.

Robert, G., & Bertsch, P. M. (1999). Distinguishing between surface and bulk dehydration-dehydroxylation reactions in synthetic goethites by high-resolution thermogravimetric analysis. *Clays and Clay Minerals*, *47*(3), 329-337.

Roden, E. E. (2003). Fe (III) oxide reactivity toward biological versus chemical reduction. *Environmental Science & Technology*, *37*(7), 1319-1324.

Sakthivel, R., Bhattacharyya, D., Eswaraiah, C., Das, D., Jayasankar, K., & Mishra, B. K. (2014). Effect of milling on reduction behavior of blue dust. *Journal of alloys and compounds*, *587*, 677-680.

Schindler, D. W., Carpenter, S. R., Chapra, S. C., Hecky, R. E., & Orihel, D. M. (2016). Reducing phosphorus to curb lake eutrophication is a success. *Environmental Science & Technology*, *50*(17), 8923-8929.

Senn, A. C., Kaegi, R., Hug, S. J., Hering, J. G., Mangold, S., & Voegelin, A. (2015). Composition and structure of Fe (III)-precipitates formed by Fe (II) oxidation in water at near-neutral pH: Interdependent effects of phosphate, silicate and Ca. *Geochimica et cosmochimica acta*, *162*, 220-246.

Shen, J., Griffiths, P. T., Campbell, S. J., Utinger, B., Kalberer, M., & Paulson, S. E. (2021). Ascorbate oxidation by iron, copper and reactive oxygen species: review, model development, and derivation of key rate constants. *Scientific reports*, *11*(1), 1-14.

Slomp, C. P., Van der Gaast, S. J., & Van Raaphorst, W. (1996). Phosphorus binding by poorly crystalline iron oxides in North Sea sediments. *Marine Chemistry*, *52*(1), 55-73.

Stookey, L. L. (1970). Ferrozine---a new spectrophotometric reagent for iron. *Analytical chemistry*, *42*(7), 779-781.

Timoshnikov, V. A., Kobzeva, T. V., Polyakov, N. E., & Kontoghiorghes, G. J. (2020). Redox interactions of vitamin C and iron: Inhibition of the pro-oxidant activity by deferiprone. *International Journal of Molecular Sciences*, *21*(11), 3967.

Udert, K. M. (2018). Phosphorus as a resource. *Phosphorus: Polluter and Resource*, *57*, 57.

USEPA. (2011). Drinking water treatment plant residuals. Available at: https://www.epa.gov/sites/default/files/2015-11/documents/dw-treatment-residuals-mgmt-tech-report-sept-2011.pdf

van der Grift, B., Rozemeijer, J. C., Griffioen, J., & van der Velde, Y. (2014). Iron oxidation kinetics and phosphate immobilization along the flow-path from groundwater into surface water. *Hydrology and Earth System Sciences*, *18*(11), 4687-4702.

Voegelin, A., Kaegi, R., Frommer, J., Vantelon, D., & Hug, S. J. (2010). Effect of phosphate, silicate, and Ca on Fe (III)-precipitates formed in aerated Fe (II)-and As (III)-containing water studied by X-ray absorption spectroscopy. *Geochimica et Cosmochimica Acta*, *74*(1), 164-186.

Wang, C., Liang, J., Pei, Y., & Wendling, L. A. (2013). A method for determining the treatment dosage of drinking water treatment residuals for effective phosphorus immobilization in sediments. *Ecological engineering*, *60*, 421-427.

Wang, J., Zhang, G., Qiao, S., & Zhou, J. (2021). Magnetic Fe0/iron oxide-coated diatomite as a highly efficient adsorbent for recovering phosphorus from water. *Chemical Engineering Journal*, *412*, 128696.

Wang, R., Wilfert, P., Dugulan, I., Goubitz, K., Korving, L., Witkamp, G. J., & van Loosdrecht, M. C. (2019). Fe (III) reduction and vivianite formation in activated sludge. *Separation and Purification Technology*, *220*, 126-135.

Wilfert, P., Kumar, P. S., Korving, L., Witkamp, G. J., & Van Loosdrecht, M. C. (2015). The relevance of phosphorus and iron chemistry to the recovery of phosphorus from wastewater: a review. *Environmental science & technology*, *49*(16), 9400-9414.

Wołowiec, M., Komorowska-Kaufman, M., Pruss, A., Rzepa, G., & Bajda, T. (2019). Removal of heavy metals and metalloids from water using drinking water treatment residuals as adsorbents: A review. *Minerals*, *9*(8), 487.

Wyant, K. A., Corman, J. R., & Elser, J. J. (2013). Phosphorus, food, and our future. Oxford University Press.

Yee, N., Shaw, S., Benning, L. G., & Nguyen, T. H. (2006). The rate of ferrihydrite transformation to goethite via the Fe (II) pathway. *American Mineralogist*, *91*(1), 92-96.

Yuan, Z., Jiang, S., Sheng, H., Liu, X., Hua, H., Liu, X., & Zhang, Y. (2018). Human perturbation of the global phosphorus cycle: changes and consequences. *Environmental science & technology*, *52*(5), 2438-2450.

Zhu, J., Li, M., & Whelan, M. (2018). Phosphorus activators contribute to legacy phosphorus availability in agricultural soils: A review. *Science of the Total Environment*, *612*, 522-537.

Appendix A – Calibration series

The upper calibration series was originally made by Mingkai Ma (*Figure A-1*), a repeat of this series using the same Fe(II) standards was performed, which is shown in the lower graph (*Figure A-2*). Given the marginal, but insignificant difference in terms of influence on the data fitting procedures, and the fact that the linearity of the original callibration series was better, the upper calibration graph was used throughout our experiments.
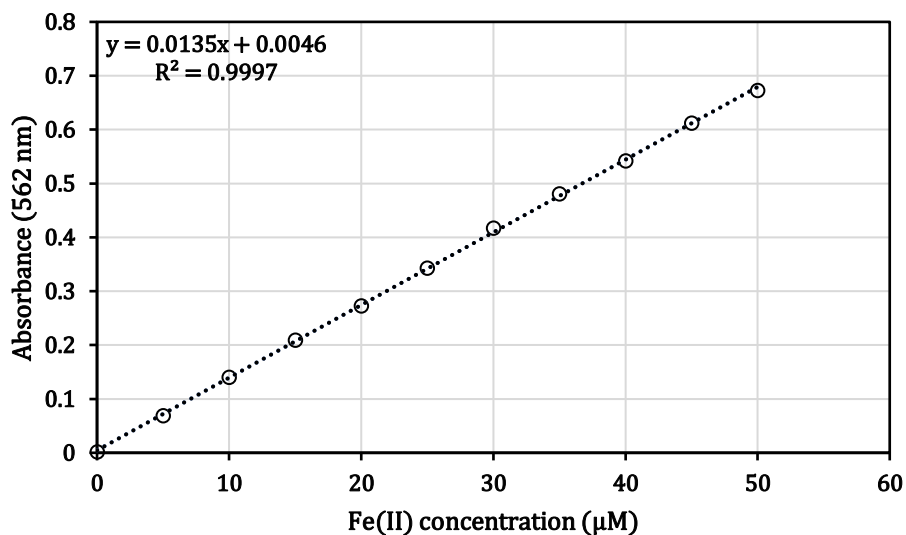

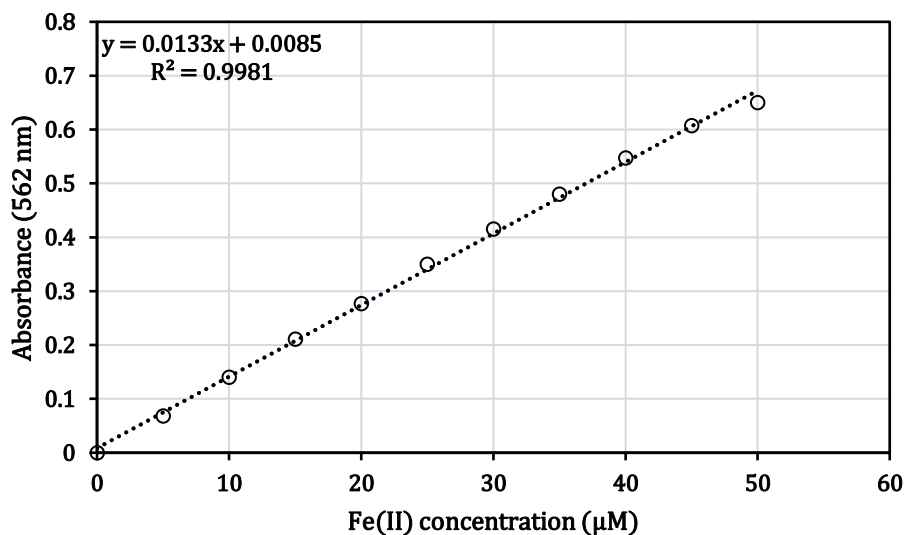Figure A-1: ferrozine callibration series performed by Mingkai Ma.

Figure A-2: ferrozine callibration series repeat performed by the author.

Appendix B – Ferrozine data transformation

An example of transforming the absorbance data (at $\lambda = 562$ nm) obtained through the ferrozine method to Fe(II) concentrations is provided in *Table B-1* below and uses data from EVHUI. First, the concentration of the solution in the measured semi-cuvette is calculated using *Equation B-1* stemming from the Fe(II) calibration series (Appendix A):

$$C_{sc} = \frac{ABS - 0.004591}{0.013493} \cdot 10^{-3} \qquad (B-1)$$

where C_{sc} is the Fe(II) concentration in mM and ABS is the absorbance. Then, C_{sc} is adjusted for the dilution factors of transferring the sample from the reactor into 10% of its own volume of 6M HCl, and further dilution in UHQ using *Equation B-2*:

$$C(t) = C_{sc} \cdot d_{fac,1} \cdot d_{fac,2} \qquad (B-2)$$

Where $C(t)$ is the Fe(II) concentration in mM in the reactor, C_{sc} the Fe(II) concentration in mM in the semi-cuvette, and $d_{fac,1}$ and $d_{fac,2}$ the dilution factors. Then, $C(t)$ together with the finally measured Fe(II) concentration in the reactor $C(t_{fin})$ is used to calculate m/m_0 with *Equation B-3*:

$$\frac{m}{m_0} = \frac{C(t_{fin}) - C(t)}{C(t_{fin})} \qquad (B-3)$$

The dilution factors may of course vary between batch experiments. Concentrations at $t = 0$ are assumed to be 0 mM for all samples, and aids in the process of parameter fitting.

Table B-1: Raw data transformation of EVHUI Fe(II) ferrozine data using equations (15), (16), and (17).

t	ABS	C_{sc}	$d_{fac,1}$	$d_{fac,2}$	$C(t)$	m/m_0
[min]	[-]	[mM]	[-]	[-]	[mM]	[-]
0	-	0	-	-	0	1.0
1	0.052	3.51E-03	1.1	10	3.86E-02	0.94
6	0.213	1.54E-02	1.1	10	1.70E-01	0.74
11	0.355	2.60E-02	1.1	10	2.86E-01	0.57
21	0.515	3.78E-02	1.1	10	4.16E-01	0.37
32	0.612	4.50E-02	1.1	10	4.95E-01	0.25
46	0.342	2.50E-02	1.1	20	5.50E-01	0.17
63	0.362	2.65E-02	1.1	20	5.83E-01	0.12
91	0.381	2.79E-02	1.1	20	6.14E-01	0.069
186	0.409	3.00E-02	1.1	20	6.59E-01	0.0

Appendix C – Sensitivity analysis

Upon analysis a possibly important double-log relationship was found between the fitting parameters *a* and *v* (*Figure C-1*). This initially raised concerns over the consistency and robustness of the data fitting procedure, as this could be indicative of multiple solutions (significantly different combinations of *a* and *v*) being possible for individual data-sets.
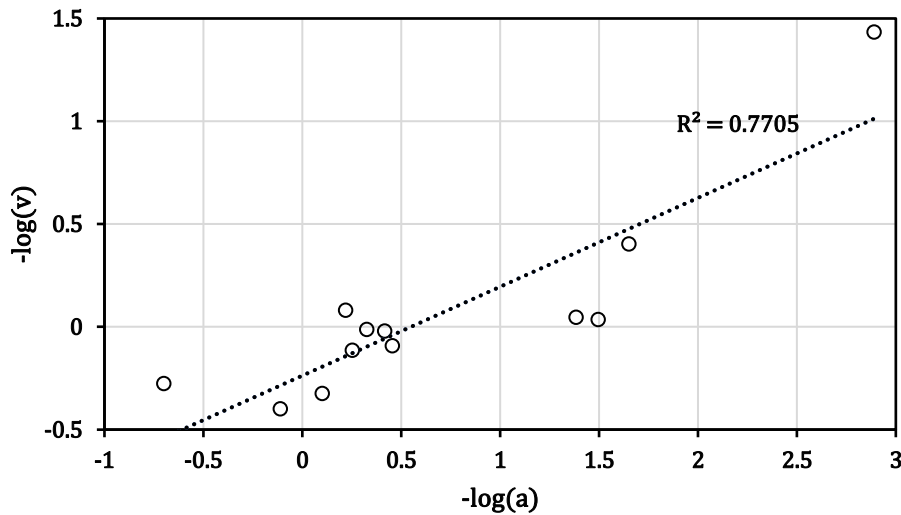

Figure C-1: double-log relationship between parameters *a* and *v* with a linear fit and R^2 value.

However, upon performing a sensitivity analysis with various initial values for *a* and *v* and keeping track of the changes in k_{app} and γ_{app}, it was determined that there was no significant variation (*Figure C-2*). Although, interestingly, the variations that were observed appeared dependant on the size of the initial values.
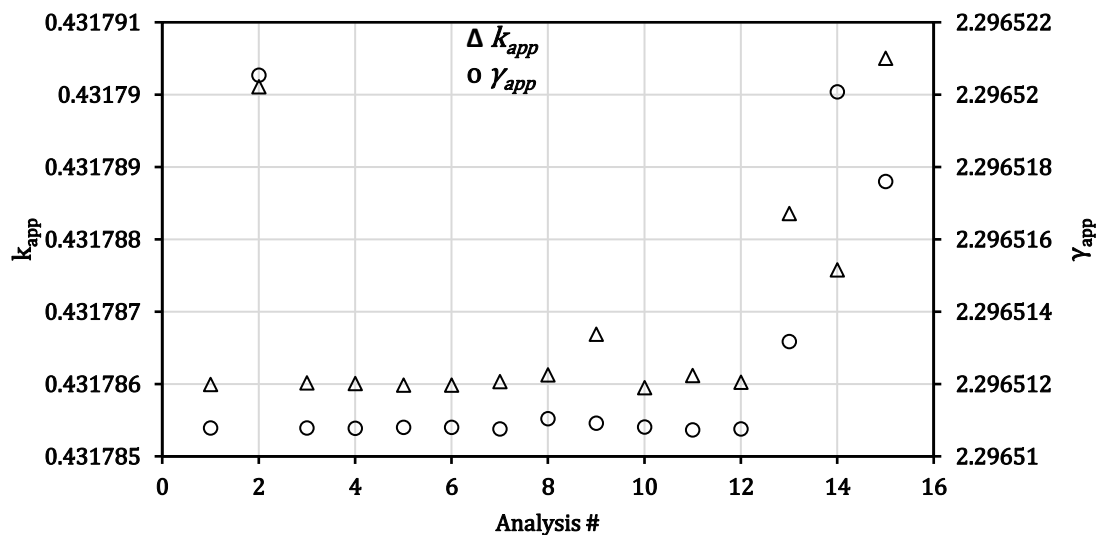

Figure C-2: graph of k_{app} and γ_{app} values changing as a result of varying initial *a* and *v* values.

Appendix D – Titration data transformation

An example of transforming the H^+ consumption data, obtained from titration, to Fe(II) concentrations is provided in the graph below and uses data from VITVEE. Although the reactor was regularly sampled, meaning the suspension volume was likely lower than 150 mL, but was assumed to be constant as there was no data available for how much volume was removed in total. For the titration, a solution of 0.1M HCl was used, which can be transformed to mol/mL and consequently multiplied with the volume of acid added at time-point t to obtain the moles of H^+ added to the reactor (*Equation D-1*).

$$moles\ H^+ =\ V_{titrant}(t) \cdot 0.0001 \qquad \text{(D-1)}$$

Then, the moles of H^+ are divided by the volume of the reactor in L, which consists of the assumed constant volume of 0.15 L together with the added volume of titrant in L, providing the concentration of H^+ in the reactor in M (*Equation D-2*).

$$H^+_{reactor} = \frac{moles\ H^+}{0.15 + V_{titrant}(t)} \qquad \text{(D-2)}$$

This allows for the calculation of Fe(II) evolution over time by simply dividing the H^+ concentration by two, according to the reaction stoichiometry provided in *Equation 14*, which produces the following graph.
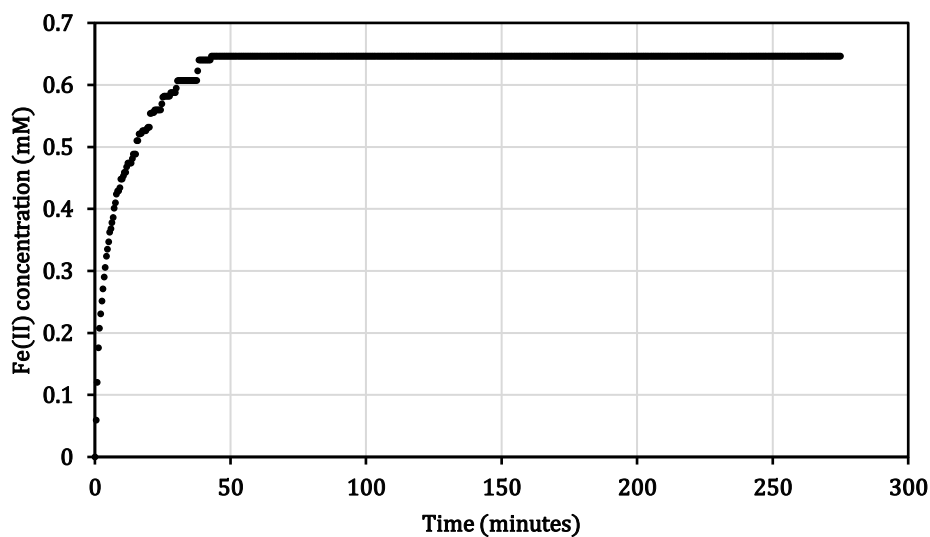

Figure D-1: Fe(II) concentration time-evolution in mM calculated from H^+ consumption data.

Appendix E – Arrhenius transformation of k_{app} values

Apparent rate constants k_{app} in this paper were determined at T = 60°C. Values in Larsen and Postma (2001) were found at T = 25°C. Rate constants can be adjusted for temperature changes using the Arrhenius equation (*Equation E-1*).

$$k(T_2) = k(T_1)e^{\frac{E_a}{R}\left(\frac{1}{T_1}-\frac{1}{T_2}\right)}$$ (E-1)

Here, $k(T_2)$ represents the rate constant to be calculated at the new temperature T_2 in s^{-1}; $k(T_1)$ the known rate constant at its respective temperature T_1 s^{-1}; T_1 and T_2 the previous temperature and the temperature we want to calculate for in Kelvin; E_a the activation energy for the respective materials in J/mol; and R at 8.314 Jmol^{-1}K^{-1}. For example, for a transformation of a rate constant for an assumed 6-line Fh containing material from T = 60°C to T = 25°C, the calculation is used according to *Equation E-2*.

$$k(T_2) = 5.8 \cdot 10^{-4}e^{\frac{60000}{8.314}\left(\frac{1}{333.15}-\frac{1}{298.15}\right)} = 4.6 \cdot 10^{-4}s^{-1}$$ (E-2)

Using the E_a values found in literature and the observed rate constants from this paper, *Table E-1* was produced.

Table E-1: rate constants of this study and Larsen and Postma (2001) compared at T = 25°C.

	$k_{2\text{-}fh}$ [s^{-1}]	$k_{6\text{-}fh}$ [s^{-1}]
This study	$4.4 - 7.2 \cdot 10^{-4}$ s^{-1}*	$4.6 - 7.4 \cdot 10^{-5}$ s^{-1}†
Larsen and Postma (2001)	$6.6 - 7.6 \cdot 10^{-4}$ s^{-1}	$7.4 \cdot 10^{-5}$ s^{-1}

* transformed using E_a = 56 kJ/mol for 2-line Fh from Yee et al. (2006)
†transformed using a nearing value E_a = 60 kJ/mol for 6-line Fh from Erbs et al. (2008)